Climatology and long-term evolution of ozone and carbon monoxide in the UTLS at northern mid-latitudes, as seen by IAGOS from 1995 to 2013

Yann Cohen[1,2], Hervé Petetin[1], Valérie Thouret[1], Virginie Marécal[2], Béatrice Josse[2], Hannah Clark[1], Bastien Sauvage[1], Alain Fontaine[1], Gilles Athier[1], Romain Blot[1], Damien Boulanger[3], Jean-Marc Cousin[1], and Philippe Nédélec[1]

[1]Laboratoire d'Aérologie, Université de Toulouse, CNRS, UPS, France
[2]Centre National de Recherches Météorologiques, CNRS-Météo-France, UMR 3589, Toulouse, France
[3]Observatoire Midi-Pyrénées, Toulouse, France

Correspondence to: yann.cohen@aero.obs-mip.fr

Abstract. In situ measurements in the upper troposphere - lower stratosphere (UTLS) are performed in the framework of the European research infrastructure IAGOS (In-service Aircraft for a Global Observing System) for ozone since 1994 and for carbon monoxide since 2002. The flight tracks cover a wide range of longitudes in the northern extratropics, extending from the North American western coast (125°W) to the eastern Asian coast (135°E), and more recently over the northern Pacific ocean.

5   Different tropical regions are also sampled frequently, such as the Brazilian coast, central and southern Africa, southeastern Asia and the western Maritime Continent. As a result, a new set of climatologies for O_3 (Aug. 1994 – Dec. 2013) and CO (Dec. 2001 – Dec. 2013) in the upper troposphere (UT), tropopause layer and lower stratosphere (LS) are made available, including quasi-global gridded horizontal distributions, and seasonal cycles over eight well sampled regions of interest in the northern extratropics. The seasonal cycles generally show a summertime maximum in O_3 and a springtime maximum in CO in the UT,

10 in contrast with the systematic springtime maximum in O_3 and the quasi- absence of seasonal cycle of CO in the LS. This study highlights some regional variabilities in the UT notably (i) a west-east difference of O_3 in boreal summer with up to 15 ppb more O_3 over central Russia compared with northeast America, (ii) a systematic west-east gradient of CO from 60°E to 140°E (especially noticeable in spring and summer with about 5 ppb by 10 degrees longitude), (iii) a broad spring/summer maximum of CO over North East Asia, and (iv) a spring maximum of O_3 over Western North America. Thanks to almost 20

15 years of O_3 and 12 years of CO measurements, the IAGOS database is a unique data set to derive trends in the UTLS. Trends in O_3 in the UT are positive and statistically significant in most regions, ranging from +0.25 to +0.45 ppb.yr^{-1}, characterized by the significant increase of the lowest values of the distribution. No significant trends of O_3 are detected in the LS. Trends of CO in the UT, tropopause and LS are all negative and statistically significant. The estimated slopes range from -1.37 to -0.59 ppb.yr^{-1}, with a nearly homogeneous decrease of the lowest values of the monthly distribution (fifth percentile) contrasting

20 with the high inter-regional variability of the highest values (95th percentile).

1 Introduction

Ozone plays an important role in the thermal structure of the stratosphere, and in the oxidizing capacity of the troposphere as a major source of hydroxyl radicals (OH). Tropospheric ozone is also a strong greenhouse gas (IPCC, 2013, AR5). In contrast with carbon dioxide (CO_2) and methane (CH_4), the scientific understanding concerning its radiative forcing (RF) is still at a

5 medium level. Nevertheless, it has been shown that its impact on surface temperature reaches its maximum when changes to O_3 mixing ratios occur in the upper troposphere - lower stratosphere (UTLS) region (e.g. Riese et al., 2012). Carbon monoxide (CO) is a precursor for CO_2 and tropospheric O_3. It is also a major sink for OH radicals in unpolluted atmosphere (Logan et al., 1981; Lelieveld et al., 2016) thus increasing the lifetime of CH_4, such that CO emissions are considered as "virtually certain" to cause a positive RF (IPCC, 2013, AR5). Because of its ~2-month lifetime (Edwards et al., 2004), it can be used

10 as a tracer of combustion processes, mainly anthropogenic emissions and biomass burning (Granier et al., 2011), although it is also a product of the oxidation of CH_4 and isoprene (C_6H_8). Identifying the contributions from different factors on O_3 concentrations in the UTLS is more difficult than for CO. First, the O_3 mixing ratio is influenced by transport from both the stratosphere (e.g. Hsu and Prather, 2009; Stevenson et al., 2013) and the troposphere (e.g. Barret et al., 2016; Zhang et al., 2016). Second, tropospheric O_3 is produced from a wide variety of precursors (NMVOCs, CO, HO_2) emitted from numerous

15 surface sources, both natural and anthropogenic. Third, nitrogen oxides (NOx) implicated in the production of O_3 are emitted not only at the surface by combustion processes, but also in the free troposphere by lightning. In parallel, NOx can be released by the decomposition of reservoir species such as peroxyacetyl nitrate (PAN), a long-lived species that can be transported at intercontinental scales in the free troposphere (e.g. Hudman et al., 2004).

Establishing trends in O_3 and CO with observations is important for evaluating the impact of the reduction of anthropogenic

20 emissions in the northern midlatitudes on the atmospheric chemical composition. It is also important for enhancing the knowledge about the role of O_3 in the increasing atmospheric radiative forcing. Furthermore, both observed trends and climatologies (i.e. time-averaged data) are used as reference values in order to evaluate the ability of models to reproduce past atmospheric composition, and thus to forecast future changes. Consequently, assessing the mean distribution and the long-term evolution of these two trace gases is within the focus of several research programs dealing with the understanding of atmospheric composi-

25 tion, regarding air quality and climate issues.

The present study is based on the measurements of these two trace gases, available in one single data set, the IAGOS database (http://www.iagos.org). In the framework of the IAGOS program (In-service Aircraft for a Global Observing System; Petzold et al., 2015), the measurements on board commercial aircraft at 9-12 km a.s.l. cruise levels provide an accurate sampling with a high frequency in the UTLS, particularly over northern mid-latitudes. With a monitoring period reaching approximately 20

30 years for O_3 and 12 years for CO in this area, the time-series based on the IAGOS data set can provide helpful information for shorter aircraft campaigns, allowing the quantification of background values as an interannually variable signal. Also, with a dense geographical coverage spreading over the mid-latitudinal zonal band (except the Pacific ocean so far as regular measurements only started in 2012), spatial distributions seen by IAGOS are a source of complementary information for local observations, quantifying the spatial variability at synoptic and intercontinental scales. The monitoring period is now sufficient

to derive representative climatologies and long-term evolution of both species over different regions of interest.

Since the 1990s, several observation systems have been monitoring these two species, aiming at a better understanding of the processes controlling their spatial distribution and temporal evolution, (multi-) decadal trends and interannual variability (IAV). Satellite-based instruments provide a global coverage but with limited vertical resolution while sondes, LiDAR (Light Detection And Ranging) and aircraft in situ measurements during ascent and descent phases offer a precise view of the vertical profile over a limited area. Neu et al. (2014b) have recently presented a comprehensive intercomparison of currently available satellite (limb and nadir viewing) O_3 climatologies in the UTLS (300-70 hPa). Although suffering from a coarse vertical resolution, such an analysis offers a basis for comparison of the large-scale spatio-temporal characteristics of the O_3 distribution (e.g. zonal mean cross sections, seasonal variability, IAV) within the UTLS. The authors point out the large differences in these satellite-based climatologies in the UTLS. A more detailed picture of the UTLS with a higher spatial and temporal resolution and multiple species is often required and can be addressed with aircraft platforms. Tilmes et al. (2010) proposed an integrated picture of O_3, CO and H_2O climatologies over northern hemisphere (mostly representative of North America and Europe) based on research aircraft campaigns. They provide a valuable data set representing the vertical gradients of H_2O, O_3 and CO in three regimes: tropics, sub-tropics, and polar region of northern hemisphere. Research aircraft have a major advantage that they may fly at high altitudes. Such a study has allowed tropopause-referenced tracer profiles and tracer-tracer correlations to further highlight the transport and mixing processes on a wider vertical range than allowed by commercial aircraft. However, the IAGOS program using commercial aircraft as a multi-species measurement platform presents the advantage of higher spatial and temporal resolution to further characterize regional differences. One of the objectives of the present study is to emphasize the use of IAGOS as a complementary database to the above-mentioned ones allowing further investigations on composition and trends in O_3 and CO in the UTLS (8-12 km) in the northern hemisphere.

Previous studies using satellite measurements have shown a significant decadal decrease in the CO column at the global scale, with a higher sensitivity in the mid-troposphere. Worden et al. (2013) found a negative trend over several northern extratropical regions with MOPITT (Measurements of Pollution in the Troposphere) and AIRS (Atmospheric InfraRed Sounder), respectively from 2000 to 2011 and from 2003 to 2011. Laken and Shahbaz (2014) derived a globally negative trend in the CO column with MOPITT from March 2000 to April 2012, despite significant increases in some tropical and subtropical regions. In the upper troposphere (UT), aircraft measurements have also highlighted regional decreases in CO concentrations. A significant negative trend was derived with MOZAIC flights (Measurements of water vapor and Ozone by Airbus In-service airCraft), over western Europe from 2003 to 2009 (Gaudel et al., 2015b). More specifically above Frankfurt airport, Petetin et al. (2016) showed a decrease in CO using IAGOS data recorded during vertical ascents and descents from 2003 to 2012. Recently, Jiang et al. (2017) suggested that the trends in CO were likely to be caused by the decrease of emissions from the US, eastern China and Europe from 2001 to 2015, despite the unchanged CO emissions since 2008 in the European region.

Recent studies concerning O_3 trends show more varied results. Based on SCIAMACHY (Scanning Imaging Absorption spectrometer for Atmospheric Chartography) tropospheric column measurements during 2003-2011, Ebojie et al. (2016) derived increases over Alaska and decreases over the North American outflow, southern Europe and Siberia. Tropospheric Ozone

Mapping System (TOMS) showed an increasing tropospheric O_3 column in both northern and southern mid-latitudal Pacific Ocean from 1979 to 2003. Neu et al. (2014a) highlighted an increase in mid-tropospheric O_3 (510 hPa) in the 30°-50° zonal band from mid-2005 to 2010. Granados-Muñoz and Leblanc (2016) derived a 1σ-significant increase between 7 and 10 km a.s.l. over Table Mountain Facility (TMF, California) from 2000 to 2015, using LiDAR measurements. Gaudel et al. (2015a)

5   combined LiDAR and ozonesondes measurements from 1991 until 2010 throughout the troposphere over Observatoire de Haute-Provence (OHP, France). From 6 to 8 km a.s.l., they found a 1σ-significant increase. The increase is also observed at the lower part of the free troposphere at some Global Atmospheric Watch stations (GAW). Most of the northern hemisphere GAW stations above 2 km a.s.l. show a significant positive trend (Oltmans et al., 2013), indicating that the increase probably takes place throughout the free troposphere. Free and upper tropospheric O_3 trends derived from various instruments are gathered

10 in the reviews of Cooper et al. (2014) and Monks et al. (2015). Amongst the in situ observations, significant positive trends since 1971 are reported from ozonesonde data above Western Europe and Japan, and also from aircraft data in the UT above northeastern USA, North Atlantic Ocean, Europe, Middle-East, southern China and Japan. More precisely during the 1990-2010 decades, ozonesonde measurements above North America and North Pacific Ocean showed positive trends. Thouret et al. (2006) showed significant positive trends for O_3 mixing ratios above eastern United States, northern Atlantic and Europe from

15 1994 to 2003 with the IAGOS data set, in the UT and the LS. The IAGOS time series is now 10 years longer and the present study brings crucial information to the interpretation of the previous trends.

Whereas the bulk of these studies show an increase in O_3 and a decrease in CO in the free troposphere, there is no available study based on in situ measurements only, in the UTLS on a decadal timescale, with a dense temporal and geographical sampling at the hemispheric scale. The objective of the present study is to examine climatologies for O_3 and CO derived from

20 the whole set of IAGOS measurements at cruise levels, as well as the trends in these two trace gases at a regional scale in the northern mid-latitudes. It is both an update and an extension of Thouret et al. (2006), with a broader climatology and longer time series from which to derive trends, and a more complete data set with the addition of CO. Today the IAGOS database allows such an analysis using regular and high resolution measurements in the UTLS spanning 19 years for O_3 and 12 years of CO. This paper aims at providing the most complete picture of the distributions of O_3 and CO at a quasi-global scale based on

25 in situ measurements. We investigate regional differences in terms of seasonal cycles and trends over northern mid-latitudes. In Sect. 2 we describe the IAGOS program, the selected UTLS definition and the methodology used to analyse the data. In Sect. 3 we present the climatologies, time series and analysis of subsequent trends.

2   Data and methodology

2.1   IAGOS data set

30 The data used in this study is provided by the IAGOS European research infrastructure (www.iagos.org; Petzold et al., 2015). IAGOS consists in automatic measurements of several trace gases and aerosols on board commercial aircraft, aiming at a better understanding of the chemical composition of the atmosphere at the global scale.

IAGOS has partly taken over the MOZAIC program (Measurement of Ozone and water vapour on Airbus In-service Aircraft;

Marenco et al., 1998). The measurements of ozone and water vapour started in August 1994 (Thouret et al., 1998; Helten et al., 1998). The measurements of CO started in December 2001 (Nédélec et al., 2003). Routine IAGOS-Core (used in this study, called IAGOS hereafter) measurements started in July 2011, with a new concept of aircraft system (e.g. near real time data transmission) and instruments (e.g. combined ozone and CO in one single analyzer, as detailed in Nédélec et al., 2015). Ozone

5   and carbon monoxide have been monitored since Aug. 1994 and Dec. 2001 respectively, with dual-beam UV and IR absorption photometers. Measurements are affected by an uncertainty range of [$\pm$ 2 % $\pm$ 2 ppb] for ozone (Thouret et al., 1998) and [$\pm$ 5 % $\pm$ 5 ppb] for CO (Nédélec et al., 2003), with a temporal resolution of 4 s and 30 s respectively.

Although the technology remained the same, the consistency between MOZAIC and IAGOS data sets raised questions and the overlapping period (2011-2014) has been used to give the users the assurance that MOZAIC-IAGOS is a unique data set

10   (named IAGOS database from now on). Indeed, it is of particular importance to make sure that the long-term evolutions of O_3 and CO distributions would not be biased by this technical change. A deep and thorough comparison between MOZAIC and IAGOS, based on several hundred vertical profiles over Frankfurt, has been summarized in Nédélec et al. (2015). The consistency between the two data sets has been demonstrated and hence, the results in the present study can be considered as independent of the transition from MOZAIC to IAGOS-Core. Thus, the recent study by Petetin et al. (2016), as well as the

15   TOAR Climate (Gaudel and Cooper, 2017, in preparation), analysis makes use of the MOZAIC-IAGOS database as a seamless one. The period of the present study spreads from the start of MOZAIC program up to December 2013, since the data from the following years are not yet fully calibrated.

2.2   Methodology

2.2.1   Definition of UT and LS

20   During each flight in extratropical latitudes, both tropospheric and stratospheric air masses are encountered. Their different properties make it necessary to distinguish between upper troposphere and lower stratosphere. Thus, we discriminate the air masses with three varying pressure intervals, i.e. the upper troposphere (UT), the lower stratosphere (LS) and the tropopause layer (TPL) as a mixing region between.

In extratropical latitudes, the discrimination between the upper tropospheric and the lower stratospheric measurement points

25   is based on the dynamical definition of the tropopause, adapted from Thouret et al. (2006): it is centered on the isosurface of potential vorticity (PV) defined as PV = 2 pvu (1 potential vorticity unit $\equiv 10^{-6} \cdot K \cdot m^2 \cdot kg^{-1} \cdot s^{-1}$). The PV values are part of the IAGOS ancillary data (http://iagos.sedoo.fr/#L4Place:) and are derived from the ECMWF operational analysis with a $1° \times 1°$ resolution, and interpolated along the aircraft trajectories. As indicated in Fig. 1, the TPL is considered as a 30 hPa-thick layer, centered on this 2 p.v.u. isosurface. The UT and the LS are defined as constant pressure intervals relative to the

30   tropopause, respectively [$P_{2\,pvu}$ + 75 hPa, $P_{2\,pvu}$ + 15 hPa] and [$P_{2\,pvu}$ - 45 hPa, $P_{2\,pvu}$ - 150 hPa]. The large pressure interval of the LS gathers all the stratospheric data points.

As mentioned above, PV values have been derived using ECMWF operational analysis. As for other ancillary data developed for the IAGOS data-set (http://iagos.sedoo.fr/#L4Place:), the up-to-date better vertical resolution of the operational analysis

since 2000 was clearly more relevant for e.g. vertical transport processes representativeness and then precision of the ancillary data. This has been in particular demonstrated for the coupling system (SOFT-IO) combining the FLEXPART Lagrangian particle dispersion model and emissions inventories to provide systematic origin of CO mixing ratio anomalies observed by IAGOS throughout the troposphere (see Sauvage et al., 2017, for further details).

5   Although this study focuses on the northern mid-latitudes, we also present briefly some results from measurements in the tropics. In the 25°S – 25°N band, the tropopause is higher than any commercial aircraft flight level, since they are bounded by the 196 hPa pressure level (below 12 km). Consequently, all the IAGOS measurement points recorded above 8 km a.s.l. are considered as belonging to the tropical UT.

2.2.2   IAGOS data analysis

10   This study gathers climatological analyses in each layer focusing on global horizontal distributions, latitudinal averages in the northern mid-latitudes, and seasonal cycles at subcontinental scales. We also present monthly time series, anomalies and subsequent long-term trends. The following paragraph summarizes the processing applied to the data for each of these analyses. Horizontal distributions from IAGOS data set are computed by gathering all the measurement points into $5° \times 5°$ cells, with respect to the season and the layer. For each cell, the average is taken into account only if the amount of measurement points

15   exceeds 2000 for O_3 and 1000 for CO over the whole period, i.e. 1995 – 2013 and 2002 – 2013 respectively. The selected size of the cells and thresholds in the amount of data ensure a good representativity of the time period, without filtering a too high proportion of data. We perform a subcontinental-scale analysis in order to take the zonal variability into account. Indeed, averages made in continental-sized regions or in zonal bands are not fitted for the IAGOS data because of the high geographical variability of the measurements. The eight regions of this study are illustrated in Fig. 1.

20   The monthly means are computed by averaging the measurement points sampled in each region for each layer. The averages are taken into account only if the amount of available data points in a month exceeds 300, and if the first and last measurements are separated by a 7 days-period at least. These selected thresholds limit the influence of short-lived events which are not representative of the whole month. The boundaries of each region are chosen as a compromise between a high level of sampling and a good representativity of the expected impact of local surface emissions and meteorological conditions.

25   The mean seasonal cycles are computed from 1995 to 2013, without taking into account the incomplete years in order to avoid biases between two seasons. In this study, the so-called incomplete years are defined as years with less than 7 available months and less than 3 sampled seasons. A threshold at 4 sampled seasons would be too restrictive, whereas a threshold at 2 would not ensure a good representativity of the whole years, especially if the sampled seasons are changing in time. With at least 7 available months a year, we make sure that most seasons are represented by more than one month. The absolute anomalies are

30   derived from the deseasonalised monthly means, i.e. the monthly means after substraction of the seasonal cycle. The relative anomalies correspond to the absolute ones, divided by the mean value of the seasonal cycle.

The trends are then computed from these anomalies, by using the non-parametric Mann-Kendall analysis combined with the Theil-Sen slope estimate (Sen, 1968). Calculations are performed with the OpenAir R package dedicated to atmospheric sciences (Carslaw and Ropkins, 2012). The Theil-Sen slope estimate corresponds to the median of the slopes defined by every

couple of points. The statistical significance is validated if the null hypothesis is rejected at a 95% confidence interval, i.e. if there is less than 5% probability that the observed long-term variability is only due to statistical fluctuations. The linear regression is based on the hypothesis that every point is independent of its neighbours. As a consequence, a positive (negative) autocorrelation can lead to an overestimation (underestimation) of the regression slope. In the aim of reducing such kinds of

5   bias, the method implemented in the OpenAir package applies a correcting factor to one half of the confidence interval depending on the autocorrelation. More details are available in the Openair Manual (https://cran.r-project.org/web/packages/openair/openair.pdf).
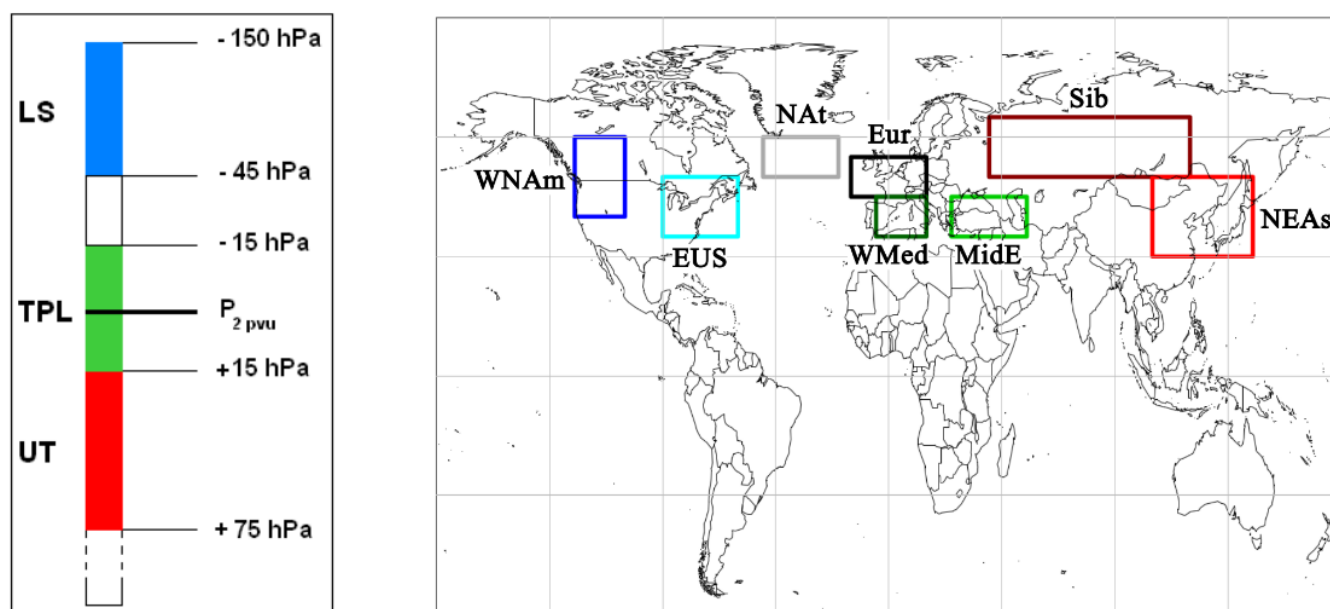
Figure 1. Left panel: Schematic representation of the definition of the upper troposphere (UT), tropopause layer (TPL) and lower stratosphere (LS) in red, green and blue respectively. The pressure levels are indicated on the right, relatively to the PV isosurface ($P_{2\,pvu}$). Right panel: Map of the regions compared in this study. From west to east: Western North America (WNAm), Eastern United States (EUS), North Atlantic (NAt), Europe (Eur), Western Mediterranean basin (WMed), Middle-East (MidE), Siberia (Sib), and Northeastern Asia (NEAs).

The statistics of IAGOS data are summarised in Tab. 1 for each region and each layer. WNAm is the least sampled region

10   ($\simeq 60\%$ of available months and $\simeq 1\,400$ flights in each layer) with a shorter time coverage per month ($\simeq 18$ days per month): consequently, a mean value computed in this region is less likely to be a representative estimation of the monthly mean volume mixing ratio (VMR). Except this one, the least sampled regions are WMed, Sib and NEAs ($\simeq 75\%$ of available months with $\simeq 3\,000$ flights in each layer), with a temporal range of 22 days per month on average. Finally, EUS, NAt and Eur are the most sampled regions ($\simeq 96\%$ of available months with $\simeq 9\,000$ flights in each layer in EUS and NAt, and more than $10\,000$ in Eur)

15   with a mean temporal range of 27 days per month.
In order to ensure a good representativeness of the measurement period for the trends analyses, we consider the best estimate

slope as realistic if the ratio of available months is higher or equal than 60%. Indeed, for each species and each layer, every region filling that condition is sampled almost from the start to the end of the measurement period (as shown later). Consequently, our analyse includes neither the trends in O_3 in the whole UTLS above WNAm nor the trends in CO in the LS above WMed.

Table 1. Regional characteristics and data statistics in each layer. The third and fourth columns refer to the proportion of available monthly data relatively to the whole period: Aug. 1994 – Dec. 2013 for O_3 and Dec. 2001 – Dec. 2013 for CO. The fifth and sixth columns indicate the total number of selected flights. The seventh and eighth columns show the time interval Δt separating the first and the last days of measurements, averaged over the available data months.

Region	Layer	Av. months (%)		Nb. of flights		Δt (days/month)	
		O_3	CO	O_3	CO	O_3	CO
Western NAm (WNAm)	LS	53	65	1 215	1 160	21	22
$\left(125 - 105°\text{W}\right.$	TPL	53	66	1 402	1 338	22	23
$\left.40 - 60°\text{N}\right)$	UT	50	66	1 471	1 438	22	23
Eastern US (EUS)	LS	94	92	8 536	3 701	27	26
$\left(90 - 60°\text{W}\right.$	TPL	94	92	10 503	4 418	27	27
$\left.35 - 50°\text{N}\right)$	UT	94	92	11 607	4 998	27	27
North Atlantic (NAt)	LS	94	92	9 125	4 149	27	27
$\left(50 - 20°\text{W}\right.$	TPL	93	91	7 706	3 488	27	26
$\left.50 - 60°\text{N}\right)$	UT	91	89	5 299	2 550	25	25
Europe (Eur)	LS	96	94	13 939	7 217	29	28
$\left(15°\text{W} - 15°\text{E}\right.$	TPL	97	94	21 162	10 812	29	29
$\left.45 - 55°\text{N}\right)$	UT	97	94	25 021	13 129	29	29
Western Med. (WMed)	LS	64	55	1 806	1 126	23	25
$\left(5°\text{W} - 15°\text{E}\right.$	TPL	69	60	2 074	1 305	23	25
$\left.35 - 45°\text{N}\right)$	UT	70	60	2 025	1 182	24	24
Middle East (MidE)	LS	89	88	3 516	2 260	24	23
$\left(25 - 55°\text{E}\right.$	TPL	88	85	3 362	2 107	24	23
$\left.35 - 45°\text{N}\right)$	UT	82	76	2 846	1 713	23	23
Siberia (Sib)	LS	76	68	4 615	2 126	26	26
$\left(40 - 120°\text{E}\right.$	TPL	76	65	3 808	1 779	26	25
$\left.50 - 65°\text{N}\right)$	UT	72	61	2 274	1 159	24	24
Northeastern Asia (NEAs)	LS	74	65	3 502	1 676	26	25
$\left(105 - 145°\text{E}\right.$	TPL	73	63	4 326	2 021	26	26
$\left.30 - 50°\text{N}\right)$	UT	76	64	4 834	2 323	27	26

3 Results

We first present the analysis of the new set of climatologies as an update of previous studies made with a shorter data set, and based on the same tropopause definition (Thouret et al., 2006; Petzold et al., 2015) as described in section 2.2.1. The present section starts with the characterisation of the seasonal distributions at the global scale. It is followed by the analysis of the

5   seasonal cycles over the eight regions defined in Fig. 1. Finally, we present the analysis of the regional long-term trends (12 years for CO, 19 years for O_3).

3.1 Horizontal distributions of O_3 and CO

Figures 2 and 3 show the 12 and 19-year seasonally averaged distribution of CO and O_3 respectively in the UT. We use the same colour scale for the four maps to highlight the seasonal and regional differences. The longitudinal distribution averaged over the

10   latitude range 25 to 75°N is projected below each map to examine the longitudinal gradients of O_3 or CO, and hypothetically highlight an intercontinental difference. The averaging interval has been chosen in order to take all upper tropospheric IAGOS measurements in the area considered here as the extratropics.

In Fig. 2, the horizontal distributions of CO mixing ratios reveal an overall spring maximum at northern mid-latitudes extending into summer over eastern Asia and northern Pacific. There are also systematic maxima in the sampled tropical regions

15   (i.e. Brazilian coast, central and southern Africa, southeast Asia), depending on their respective dry seasons. These features characterize the combination of the two most important sources, namely the anthropogenic emissions and the boreal/tropical biomass burning. At northern mid-latitudes, in contrast with near-surface observations (e.g. Zbinden et al., 2013), the averaged CO mixing ratio is higher during spring in the UT. During winter, the weaker convection and the longer lifetime of CO allow the accumulation of this trace gas in the lower troposphere despite the stronger wintertime frequency of warm conveyor belts

20   (e.g. Madonna et al., 2014), thus leading to a climatological maximum spread from late winter until early spring (Petetin et al., 2016). As the convection activity increases, the CO confined in the lower troposphere starts being uplifted to the UT. During summer, CO is less abundant in the lower layers, and the photochemistry reaches its maximum, acting as a major sink for CO by OH attack (e.g. Lelieveld et al., 2016). In the tropics, the local maxima take place during SON over the Brazilian coast, during the whole year over tropical Africa and during JJA-SON over the Bay of Bengal-southeast Asia. The maxima over

25   tropical Africa are shifted northward during MAM and southward during SON. These local maxima observed in the UT are not necessarily correlated with the dry seasons when biomass burning emissions are enhanced, because surface emissions are uplifted more efficiently during the wet seasons within deep convection (Liu et al., 2010). Further details on the distribution of CO and O_3, as seen by IAGOS, may be found in Sauvage et al. (2005, 2007a, 2007c) and Yamasoe et al. (2015). Globally, the highest values are recorded over eastern Asia (up to 170 ppb), northern Pacific (165 ppb), North America (150 ppb), sub-

30   tropical Africa (145 ppb) and the Brazilian coast (145 ppb). These regional maxima are also shown with the climatology of MOPITT total column from 2001 to 2012 (Osman et al., 2016) and MLS mixing ratio at 215 hPa (Huang et al., 2016). The main difference with the MLS climatology by Huang et al. (2016) lies in the springtime and summertime maxima over eastern Siberia and Manchuria observed by IAGOS only. The possible reasons are the 5 km vertical resolution of MLS regarding CO

mixing ratio in the UTLS, or the fact that the altitude level at 215 hPa in the extratropics generally belongs to our definition of the lower stratosphere.

Seasonal maxima highlighted in these decadal climatologies are consistent with extreme CO events already recorded in

5 the UT over eastern Asia (Nédélec et al., 2005), northern Pacific (Clark et al., 2015) and downwind of Alaskan forest fires (Elguindi et al., 2010), and in the LS downwind of Alaska and Yukon right to the eastern coast of the Atlantic ocean (Cammas et al., 2009). All of them were originating from intense biomass burning.

In the northern extratropical UT, the common characteristic of the four seasons lies in the eastward increase of climatological CO mixing ratio, from 60°E to 135°E. The difference in CO mixing ratios reaches $\simeq$ 20 ppb during fall and winter, and $\simeq$

10 40 ppb during spring and summer. There is also a low decrease from 120°W to 60°E, $\simeq$ 20 ppb in spring and within 10 ppb during the rest of the year. It is likely the resulting combination of stronger emissions from both anthropogenic and biomass burning over the Asian continent (e.g. Jiang et al., 2017), and an efficient vertical transport over there (Madonna et al., 2014; Huang et al., 2016).
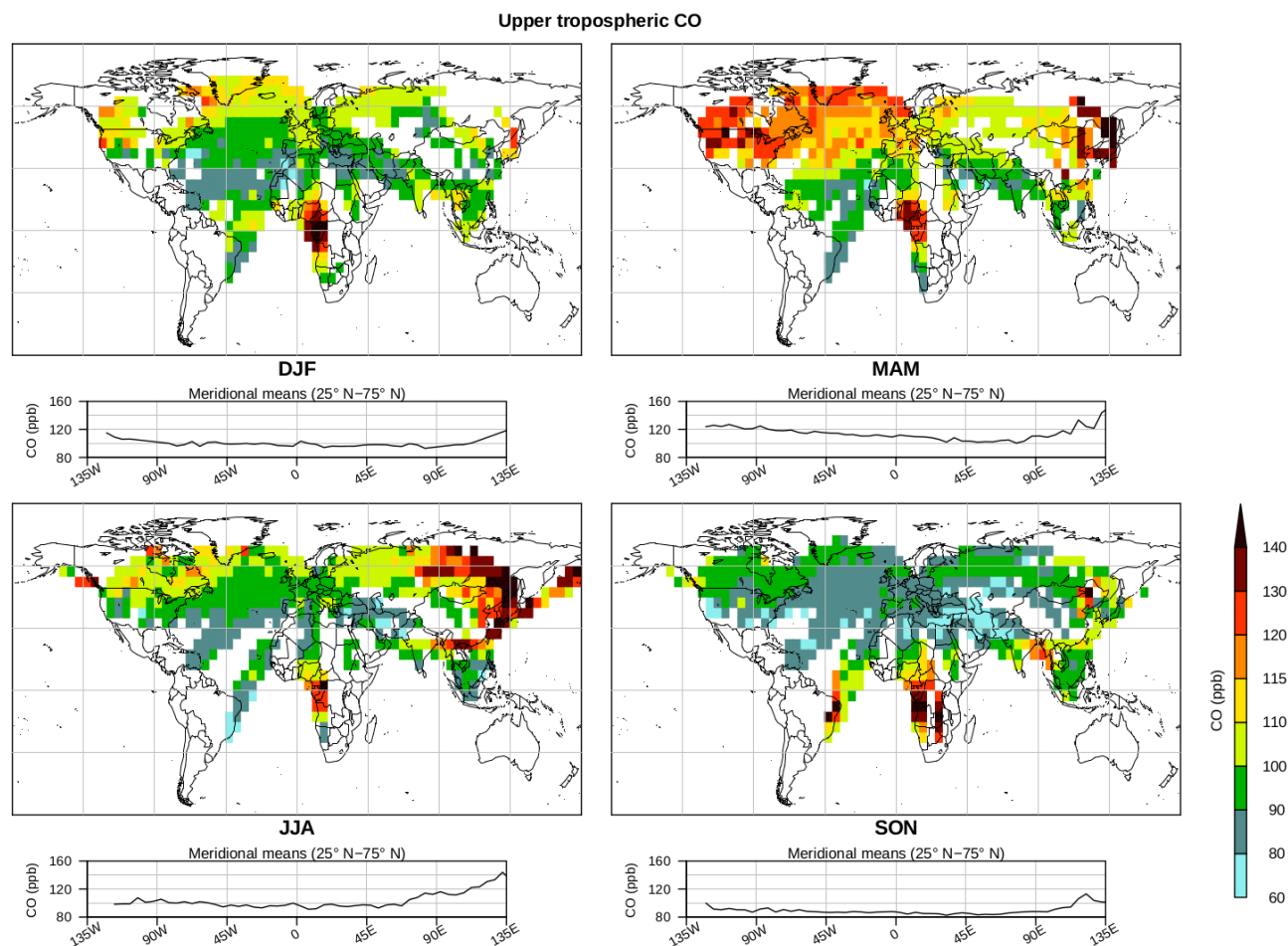
Figure 2. Horizontal distributions of CO volume mixing ratios in the UT averaged from December 2001 to November 2013, for each season. Each 2D distribution is projected on the zonal axis below, with a meridional average of the northern extratropical zonal band (from 25°N to 75°N). The 2D (respectively 1D) distributions have a 5° × 5° (respectively 5°) resolution. The grid pattern is 30°-sized in latitude, and 45°-sized in longitude. Note the larger color interval from 60 to 80 ppb, and the smaller intervals from 110 to 120 ppb.

The 20-year seasonal distribution of O_3 in the UT is shown in Fig. 3. The longitudinal variability is more detailed in the projections below the 2D distributions, where the 5° per 5° seasonal means are meridionally averaged from 25 to 75°N. At northern mid-latitudes, ozone clearly exhibits a minimum during Winter (47 ppb on average in the 25°N – 65°N zonal band) and a maximum during Summer (79 ppb), characterizing the seasonal peak of photochemical activity.

5   The highest values exceed 90 ppb over Siberia and northeastern China, while minima lower than 30 ppb are located on both sides of equatorial Pacific, at least during the wet seasons (i.e. from December until February on the western South American coast, and from December to March in the Maritime Continent). In the northern hemisphere, all over the year, O_3 mixing ratio is higher on the eastern half of the extratropical zonal band: the annual mean in the Asian continent (30 – 140°E) is 11% higher than in the western part (125°W – 15°E).

In the southern hemisphere, the SON maximum over the Brazilian coast mostly reflects the influence of lightning in South America (Bremer et al., 2004; Sauvage et al., 2007b; Yamasoe et al., 2015). The minima observed at both sides of the equatorial Pacific ocean during the respective wet seasons can highlight the strong convection of low-ozone air masses from the tropical marine boundary layer, typically ranging from 10 to 30 ppb (e.g. Thompson et al., 2003).

The satellite-based instruments Scanning Imaging Absorption Spectrometer for Atmospheric Chartography (SCIAMACHY) and Ozone Monitoring Instrument-Microwave Limb Sounder (OMI-MLS) provided climatologies of tropospheric O_3 column, averaged respectively from 2003 to 2011 and from October 2004 to December 2010. They both showed a springtime maximum, and a geographical maximum over the Atlantic ocean between $30°$ and $45°N$, which is due to STE events and surface transport of pollution from eastern USA during spring and summer (Fig. 1 in Ebojie et al., 2016; Figs. 5a-c in Ziemke et al., 2011). The discrepancies with the IAGOS climatologies can be due to uncertainties involving the stratospheric signal, i.e. the ozone stratospheric column, the height of the tropopause, and the total ozone column (Ebojie et al., 2014). The summertime climatology of O_3 mixing ratio at 464 hPa provided by Tropospheric Emission Spectrometer (TES) from 2005 to 2010 in Verstraeten et al. (2013, Fig. 1) shows similar features with IAGOS climatology. The O_3 mixing ratios are higher above the Asian continent than west of $15°E$, and there is a local maximum above Manchuria (northeastern China). In the tropics, the maximum over equatorial Africa and the minimum above and east of the Maritime continent are also seen by TES. At least in the extratropics, the altitude range observed with TES corresponds to 100-150 hPa below the lower limit of our definition of the UT. Thus, during summer, the properties we observe in the UT may extend downward, representing a wider upper part of the free troposphere.

In the tropics, Livesey et al. (2013) used Aura-MLS observations at 215 hPa since 2004 until 2011. They highlighted CO maxima over India and southeast Asia during July-August, northern equatorial Africa in February-April, southern equatorial Africa in September-November, and equatorial Brazil in October-November. According to their study and references therein, the two maxima over Asian regions are linked with anthropogenic emissions uplifted to the tropical UT by strong convection (Jiang et al., 2007), whereas the other maxima originated from biomass burning. Except for India where few summertime IAGOS data do not allow the comparison, all these maxima are consistent between MLS and IAGOS data sets. Besides, O_3 maxima are also shown by MLS above subtropical Brazil and southern subtropical Africa during September-November. Last, the climatological means they derived reached their geographical minima all along the equatorial Pacific ocean ($15°S-15°N$), which is consistent with the overall minima observed by IAGOS at both sides of the equatorial Pacific ocean.
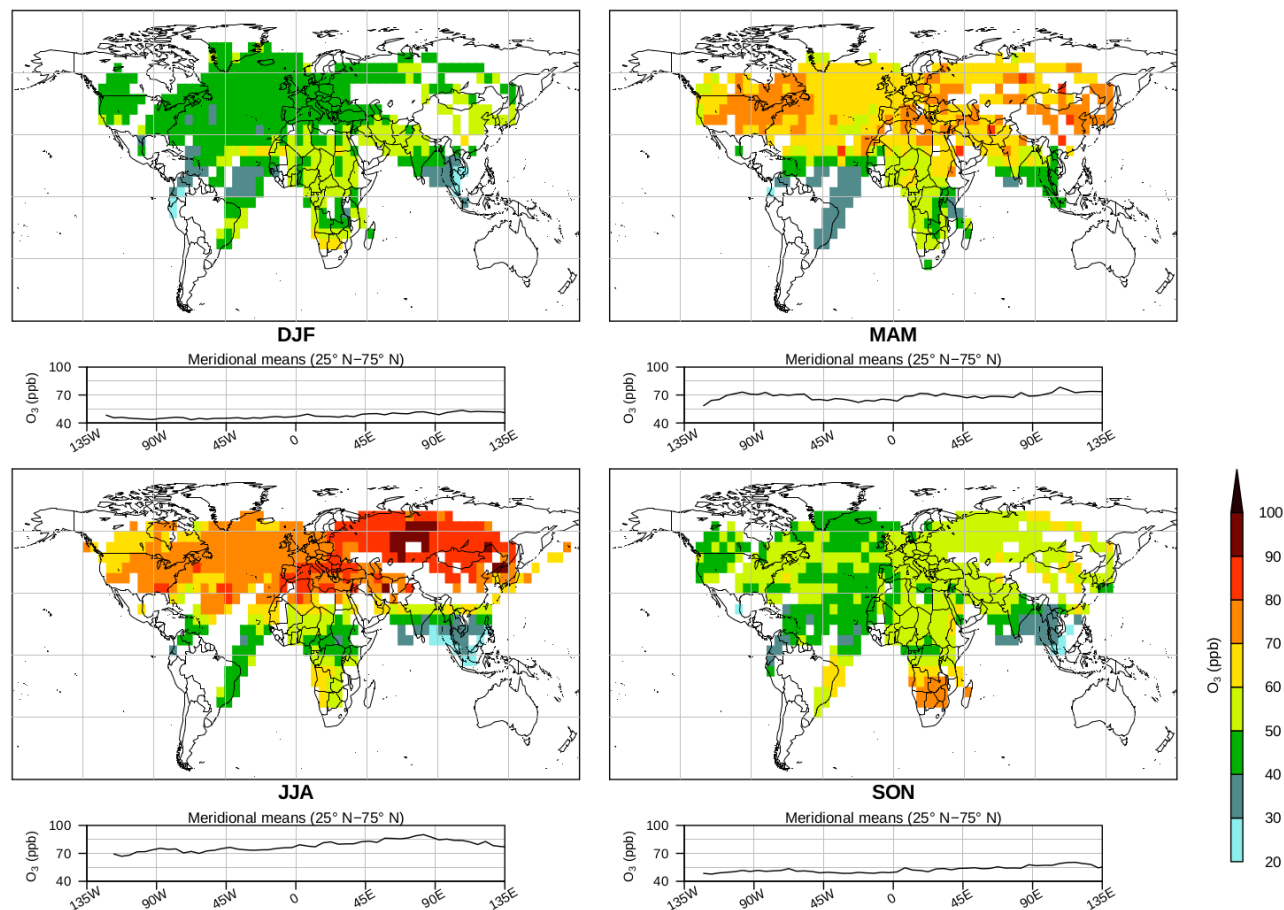
Figure 3. Horizontal distributions of O_3 volume mixing ratios in the UT averaged from December 1994 to November 2013, in every season. Each 2D distribution is projected on the zonal axis below, with a meridional average of the northern extratropical zonal band (from 25°N to 75°N). The 2D (respectively 1D) distributions have a 5° × 5° (respectively 5°) resolution.

The horizontal distribution of the O_3 mixing ratios in the LS is presented in Fig. 4. It contrasts with the upper tropospheric distribution, thus confirming the present definition of tropopause as a realistic transition layer between the troposphere and the stratosphere. The lower stratospheric climatology is characterized by a strong maximum during Spring (approximately 33% more than the annual concentrations). It originates from the January-February maximum of the downward O_3 flux at $\theta = 380$ K

5   both driven by the Brewer-Dobson circulation (BDC), and by the stratospheric photochemistry which activates at the end of winter. This feature is followed by approximately 100 days of transport until reaching the tropopause (Olsen et al., 2004). In the low latitudes of the northern extratropics, the distribution shows a poleward gradient, consistent with the adiabatic transport between the tropical UT and the extratropical lowermost stratosphere. During all seasons but autumn, the highest values are observed over Canada-Greenland and northern Siberia. During spring, these results are coherent with the climatology of the

downward 380 K O_3 flux shown in Olsen et al. (2013, Fig. 5), where observations of O_3 mixing ratio in the stratosphere (θ = 380 K) from Microwave Limb Sounder (MLS) are combined with MERRA reanalysis meteorological fields.
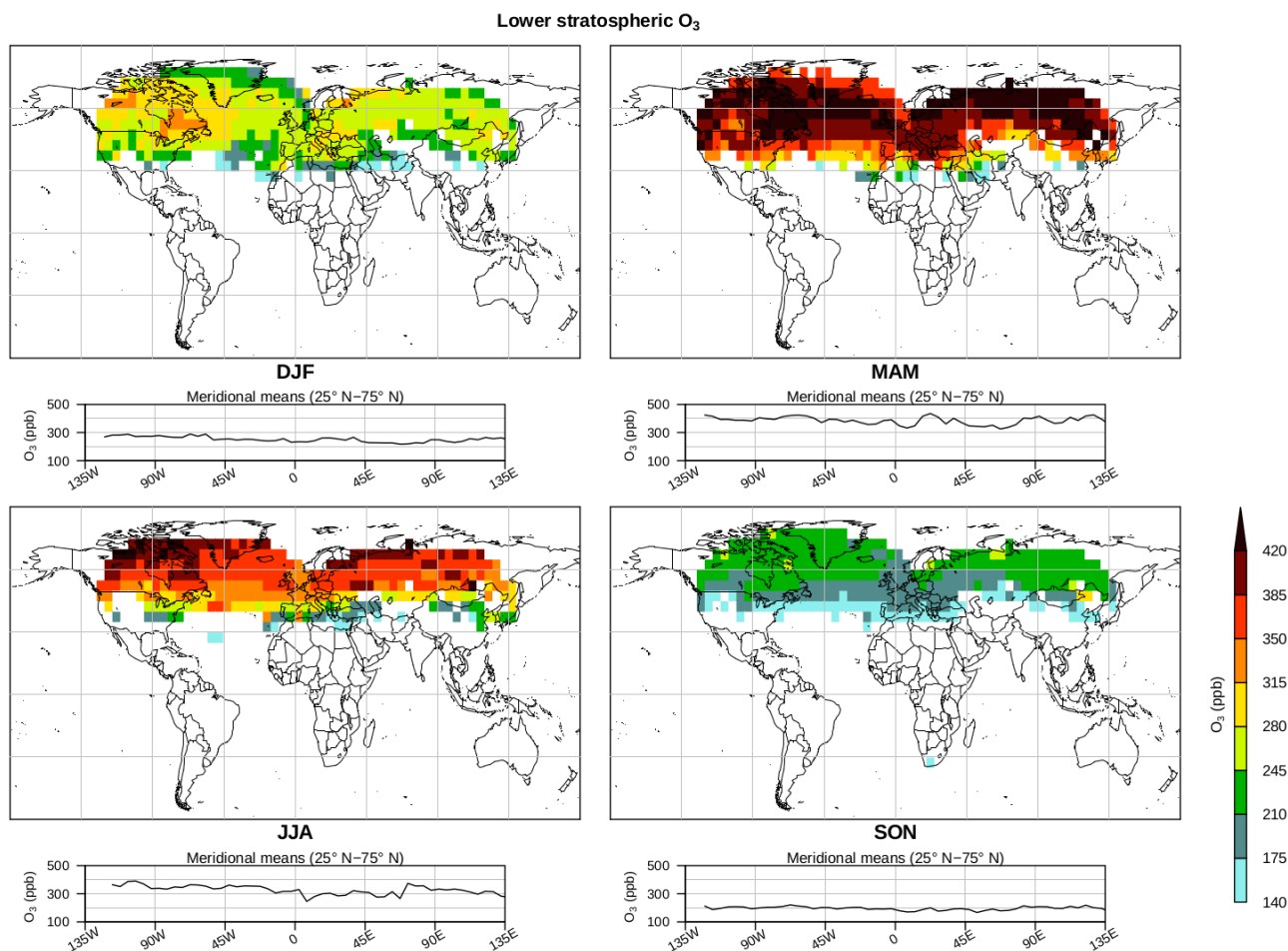
Figure 4. Same as Fig. 3, in the LS. As explained in section 2.2.1, there is no data in the subtropical stratosphere.

3.2 Regional seasonal cycles

In order to further assess the regional variability of O_3 and CO mixing ratios, we analyzed the time-series of the eight regions displayed in Fig. 1 and defined in Tab. 1. We first compare the mean seasonal cycles, before characterizing and analysing the anomalies and then, derive the trends.

In order to make a first estimate of the interregional variability of the two trace gases, the distributions of monthly means of mixing ratios during the whole monitoring period are shown in Fig. 5. Completary information is shown in Figs. 6 and 7, representing the seasonal cycles of O_3 and CO respectively, for the monthly fifth percentile (P5), mean value and 95th percentile

(P95).
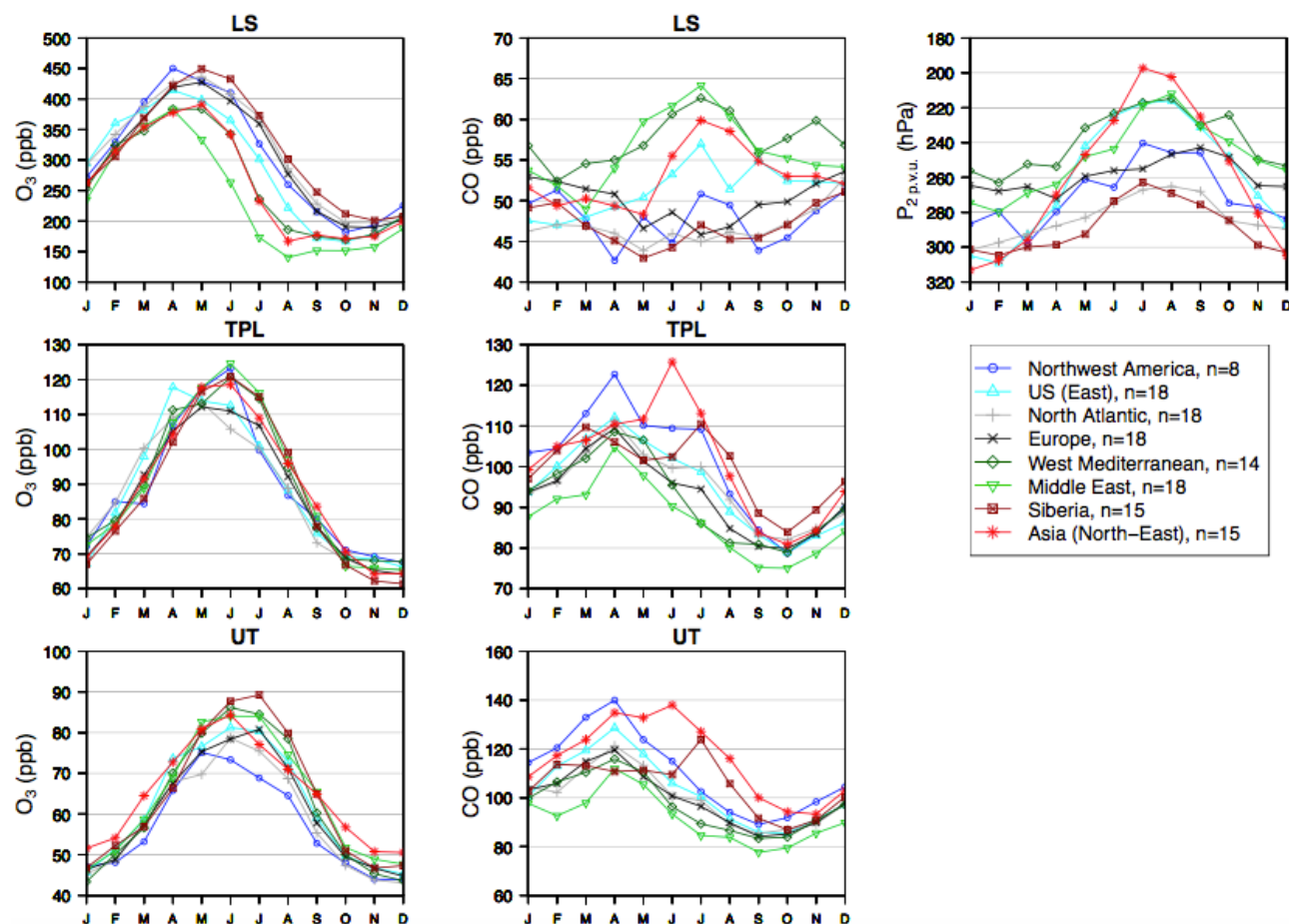
Figure 5. Mean seasonal cycles of O_3 (left panels) and CO (central panels) in the UT, TPL and LS (from bottom to top), and seasonal cycles of $P_{2\,pvu}$ (top right panel). The amount of years taken into account in the calculation of the ozone cycles is indicated in the legend.

On the left panels, O_3 shows a similar seasonal cycle for all regions. The seasonal maximum generally takes place in June-July in the UT, May-June in the TPL and April-May in the LS. This feature highlights a seasonal cycle in the TPL halfway between upper tropospheric and lower stratospheric cycles, and confirms again the tropopause definition used here as a realistic transition between the troposphere and the stratosphere.

On the middle panels, seasonal cycles for CO show a broader range of variability within the regions. The five western regions (WNAm, EUS, NAt, Eur and WMed) exhibit a spring maximum and a fall minimum in the UT and in the TPL. Asian regions (Sib, NEAs) present a different behavior in the UT with a broad spring-summer maximum. Northwest America is noticeable with the highest mixing ratios recorded from November to April. Siberia shows a significant maximum in July. In most regions, there is no noticeable seasonal variation in the LS. The right panel shows the pressure altitude of the 2 pvu isosurface

characterizing the altitude of the tropopause. As expected, all regions present a higher tropopause in summer. Besides, it is interesting to note the north-south gradient of the tropopause height. Sib (WMed), the northernmost (one of the southernmost) region(s) is presenting the lowest (highest) tropopause altitude.

5   On average, the upper tropospheric O_3 VMR varies from 46 ppb in December-January to 81 ppb in June-July, while the upper tropospheric CO VMR varies from 87 ppb in September-October to 123 ppb in April. The lower stratospheric O_3 VMR varies from 180 ppb in October-November to 410 ppb in April-May, whereas the averaged lower stratospheric CO VMR does not exhibit any seasonal cycle. The summertime maxima observed above most of the regions in the UT are likely to be driven by strong photochemistry. Indeed, Stratmann et al. (2016) used IAGOS-CARIBIC data set to compute a climatology for
10   nitrogen oxides (NOx) and their reservoir species (NOy) from 2005 until 2013, with the same definition for the UT. The regions they defined as Europe and North Atlantic are the most sampled ones in CARIBIC data set, which allows us to compare the seasonal cycles they derived in these regions with ours. Their study is based on larger regions than the ones we defined. Still, they derived upper tropospheric NO and NOy maxima well correlated with the O_3 maxima from our study. It is consistent with the leading role of photochemistry in the summertime O_3 maximum, at least in these two regions. Furthermore, Gressent et al.
15   (2014) highlighted the influence of springtime and summertime lightning activity, WCBs and convection over North America on the O_3 enhancement in the UT over North Atlantic and Europe from 2001 to 2005.

Beside these general features, the following subsections highlight some particular and local characteristics.

3.2.1   Northeast Asia, western North America and Siberia

The CO seasonal cycle in the UT over NEAs is very different from the others. Among all the regions, NEAs shows the highest
20   mixing ratios during May-September. The CO maximum is up to 140 ppb, compared to the April climatological mean from most regions around 120 ppb. Its maximum lasts from April to June. It is driven by two peaks in the percentile 95 (see the Fig. 7), one in April and one in June. The peak in April is likely due to a strong wintertime CO accumulation in the lower troposphere (Zbinden et al., 2013), strong springtime agricultural fire emissions (Tereszchuk et al., 2013) and boreal biomass burning emissions (Andela et al., 2013). The peak in June can be associated with anthropogenic and biomass burning emissions
25   coupled with geographically more frequent WCBs (e.g. Madonna et al., 2014; Nédélec et al., 2005) and summertime Asian convection (Huang et al., 2016). A similar peak is found in the TPL too, and in the LS to a lesser extent. High summertime CO VMRs are also observed over eastern Asia by MLS observations at 215 hPa (Huang et al., 2016), slightly above the TPL.

The mean upper tropospheric CO in Sib. shows a leveling off from February to June and peaks in July, like the P95 (see the Fig. 7). This is consistent with GFED and GFAS inventories that show a peak during July for CO emissions from Asian boreal
30   forest fires (Andela et al., 2013). Since the peak is noticeable in the TPL too, it may suggest a non negligible impact of pyro-convection (Tereszchuk et al., 2013).

In contrast with the other regions, the upper tropospheric O_3 seasonal cycle in WNAm does not exhibit a summertime maximum. On the contrary, the seasonal pattern common with the other regions breaks at June and July, with mean values approximately 10 ppb lower on average. NEAs is also affected by an early decrease in July. These two Pacific-coast regions

show an early decrease in the seasonal cycles of the P5 too, down to very low values in July: 32 ppb and 42 ppb respectively (Fig. 6). Meanwhile, the P5 averaged among the other regions reaches 53 ppb. This is consistent with the study of Zbinden et al. (2013), which highlights that the free troposphere above Los Angeles (118.17°W, 34.00°N) and visited Japanese airports (Osaka, Nagoya, Tokyo: 35°N, 138°E approximately) is influenced by a seasonal change in wind directions. During summer,

5   the Asian monsoon and northern American monsoon contribute to poor-O_3 air masses from subtropical Pacific ocean. LiDAR measurements over TMF during summer in 2013-2014 also showed the influence of these air masses, notably between 9 and 12 km a.s.l. (Granados-Muñoz et al., 2017). It is worth noting that despite the common characteristics with TMF, the WNAm region is located above 40°N. Thus, in contrast with TMF, WNAm may not be impacted by the rich-NOx air masses originating from Central America (Cooper et al., 2009, Fig. 7), where a strong summertime lightning activity and the North American

10   monsoon anticyclone allow the buildup of a recurrent maximum in O_3 in the UT (e.g. Cooper et al., 2007). Cooper et al. (2007 and 2009) also showed the impact of mid-latitudinal Eurasian emissions on free tropospheric O_3 above several American sites, potentially representative of the northern part of WNAm. This could explain the fact that summertime P95 in O_3 (Fig. 6) is similar to polluted regions, despite the absence of nearby sources upwind and the more frequent clean tropical air masses. It is consistent with the strong maxima of P95 for CO in WNAm (Fig. 7), correlated with the ones from NEAs. These correlated

15   maxima in April and June suggest these two regions have common upwind strong emissions. It is weaker in WNAm than in NEAs, highlighting the decrease of CO mixing ratio during the long-range transport, probably due to dilution and photochemistry.

Interestingly, in the UT, WNAm shows one of the lowest mean springtime O_3 mixing ratios too, rather linked with the upper values (see the low P95 during February-April in Fig. 6), whereas its mean springtime CO is the highest (Fig. 7). This last

20   feature is characterized by a distribution shifted toward the upper values, compared to the other regions. The lower P95 in O_3 associated with the stronger P5 in CO during February-April likely indicates that WNAm is less frequently impacted by rich-O_3 air masses, and less frequently impacted by poor-CO air masses. Lower stratospheric O_3 also exhibits the strongest P5 in WNAm, amongst all the regions. Since this feature only takes place during March-April, it is unlikely driven only by the aircraft flight level, relative to the tropopause. Furthermore, the $P_{2\,pvu}$ averages are not at lower altitudes during April. Con-

25   sequently, the stronger P5 in WNAm suggests less frequent tropospheric air masses in the LS during March-April. All these features seem to indicate less frequent springtime STE events in WNAm.

3.2.2   Western Mediterranean basin and Middle-East

As expected, the mean O_3 (CO) concentrations in the LS are lower (higher) in WMed, MidE and NEAs, which are the south-

30   ernmost regions of this study. Indeed, as the dynamical tropopause is generally higher there (Fig. 5, top right panel), the flights are likely to sample air masses closer to the tropopause, classified LS but closer to the lower boundary: the substantial difference in O_3 mixing ratios is thus explained by its strong vertical gradient in the stratosphere. However, it does not explain the difference between MidE and the two other regions during summer. At this time of the year, CO mixing ratios are similar over WMed and MidE, but MidE O_3 is significantly lower. This feature is consistent with the mixing ratios derived from OMI-MLS

observations at 150 hPa presented in Park et al. (2007) and at 100 hPa in Park et al. (2009). In southern Asia, polluted surface air masses are uplifted by deep convection during the Asian Monsoon, up to the tropical UT. The western part of the anticyclonic circulation then transports poor-O_3 air masses northward and horizontally (Barret et al., 2016). This may impact the LS in MidE (Park et al., 2007), consistent with CH_4 measurements from IASI and AIRS and modelling with the CTM MOCAGE and the CCMs CNRM-AOCCM and LMDz-OR-INCA (Ricaud et al., 2014). The summertime lower stratospheric CO VMR is comparable between WMed, MidE and NEAs. The last one is impacted by frequent WCB coupled with a strong fire activity (Madonna et al., 2014; Jiang et al., 2017).

In the UT, there is more O_3 and less CO in WMed and MidE, thus characterizing the stronger summertime subsidence at these latitudes. In MidE particularly, Etesian winds interact with the Asian Monsoon Anticyclone (AMA), enhancing the subsidence of high-level air masses (e.g. Tyrlis et al., 2013) thus allowing a recurrent summertime O_3 pool down to the mid-troposphere (Zanis et al., 2014).
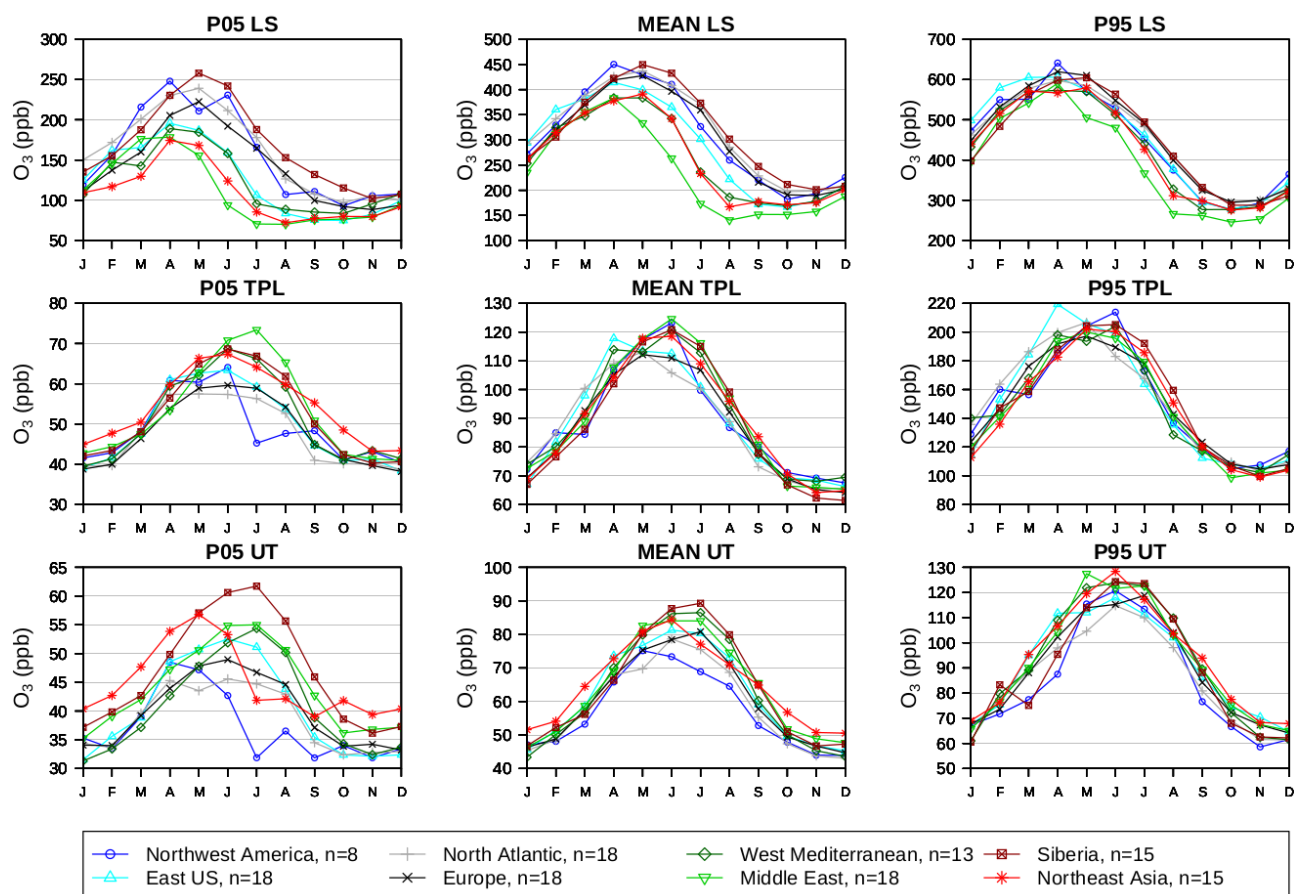
Figure 6. Seasonal cycles of O_3 for the fifth percentile (left panels), mean values (central panels) and the 95th percentile (right panels) in the UT, TPL and LS (from bottom to top). The amount of years taken into account in the calculation of the O_3 cycles is indicated in the legend.
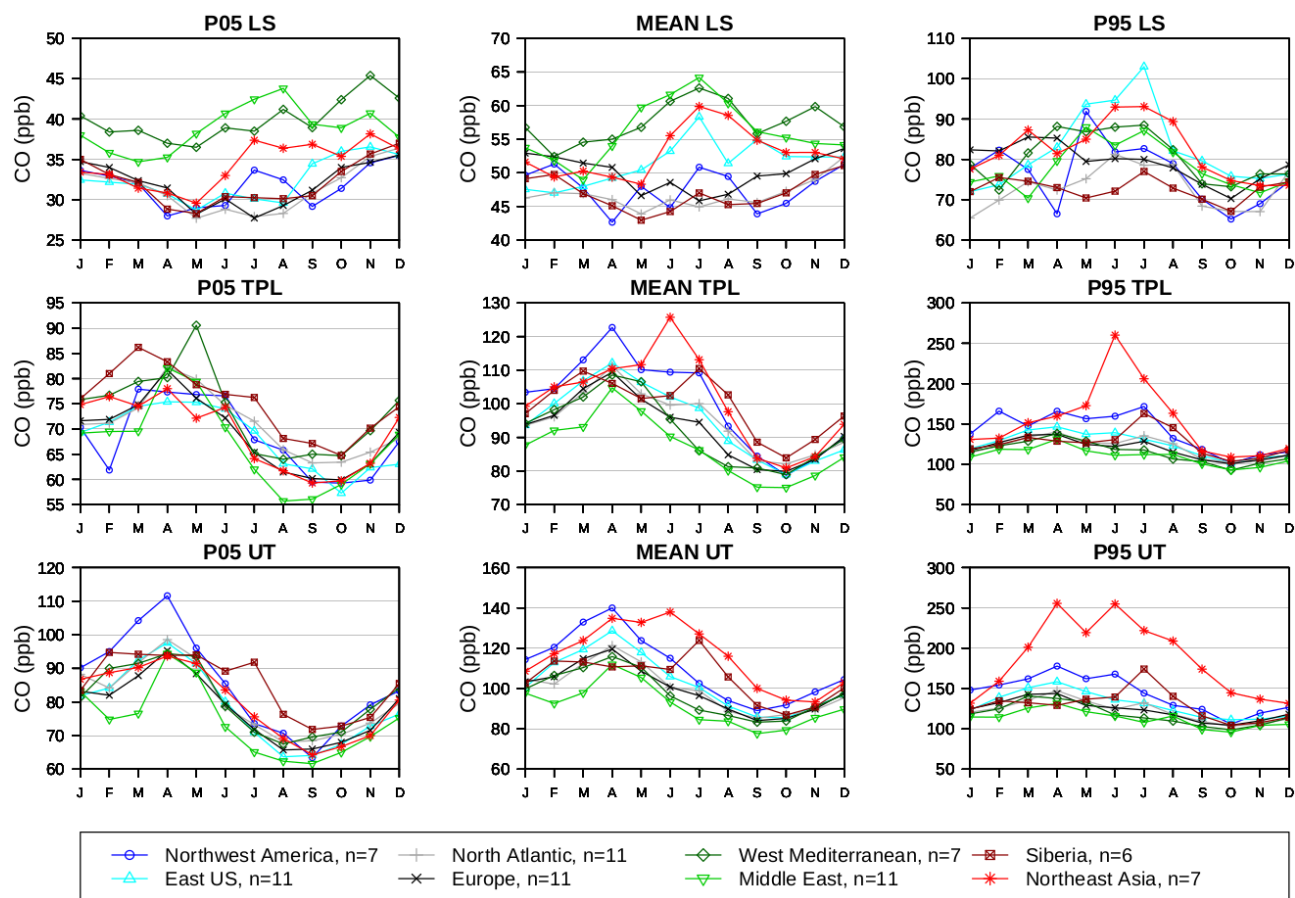
Figure 7. Seasonal cycles of CO for the fifth percentile (left panels), mean values (central panels) and the 95th percentile (right panels) in the UT, TPL and LS (from bottom to top). The amount of years taken into account in the calculation of the CO cycles is indicated in the legend.

3.3 Trends: comparison, characterisation

In this section, annual and seasonal trends of O_3 and CO are investigated in the different regions (see Sect. 2.2.2 for details on the calculations of trends), from August 1994 until December 2013 for O_3 and from December 2001 until December 2013 for CO. First, we present the corresponding time series for both species in the three layers in Figs. 8 – 13.

Upper tropospheric O₃
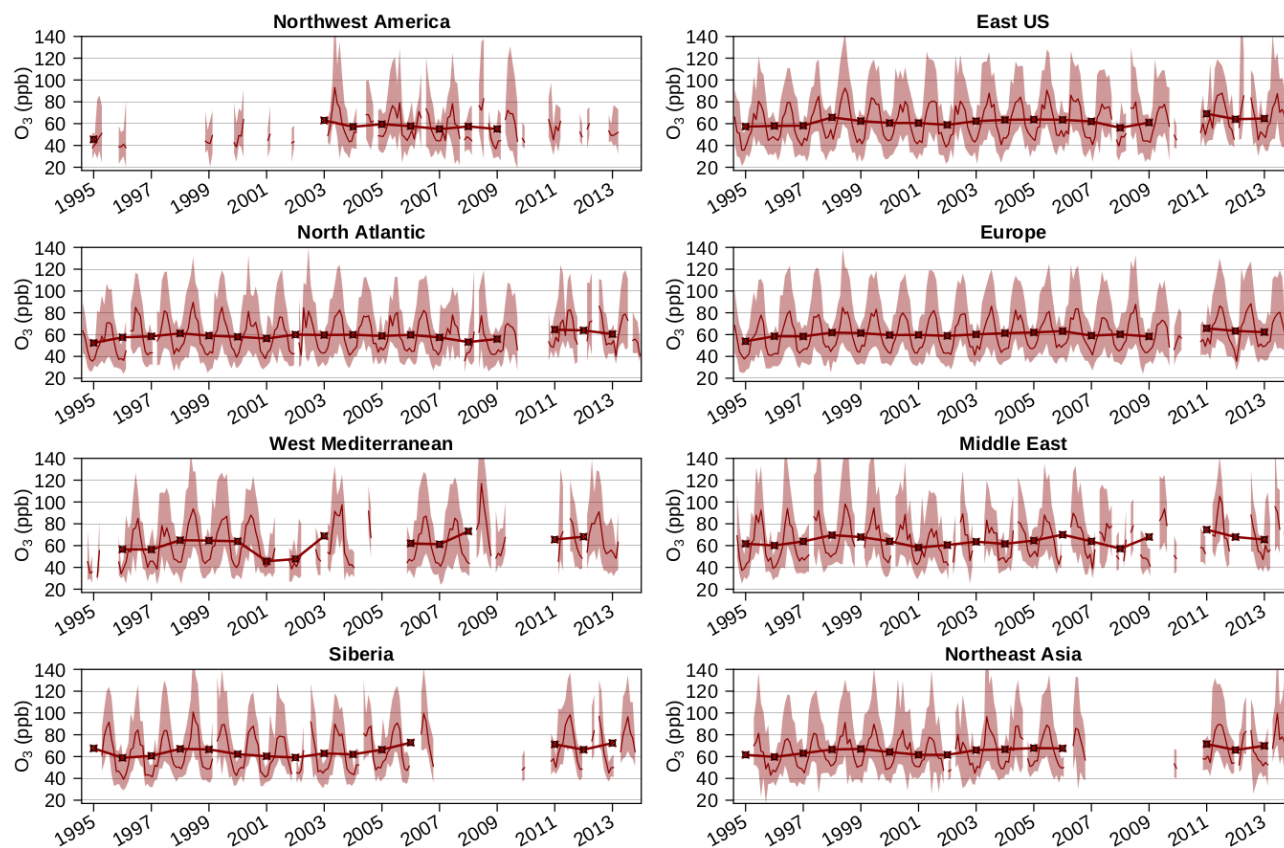
Figure 8. O₃ monthly mean values in the UT (thin curve). The interval from fifth and 95th percentiles is filled in red. The yearly mean values are represented by the bold curve and the black points.

Figure 9. O$_3$ monthly mean values in the TPL (thin curve). The interval from fifth and 95th percentiles is filled in green. The yearly mean values are represented by the bold curve and the black points.

Lower stratospheric O$_3$
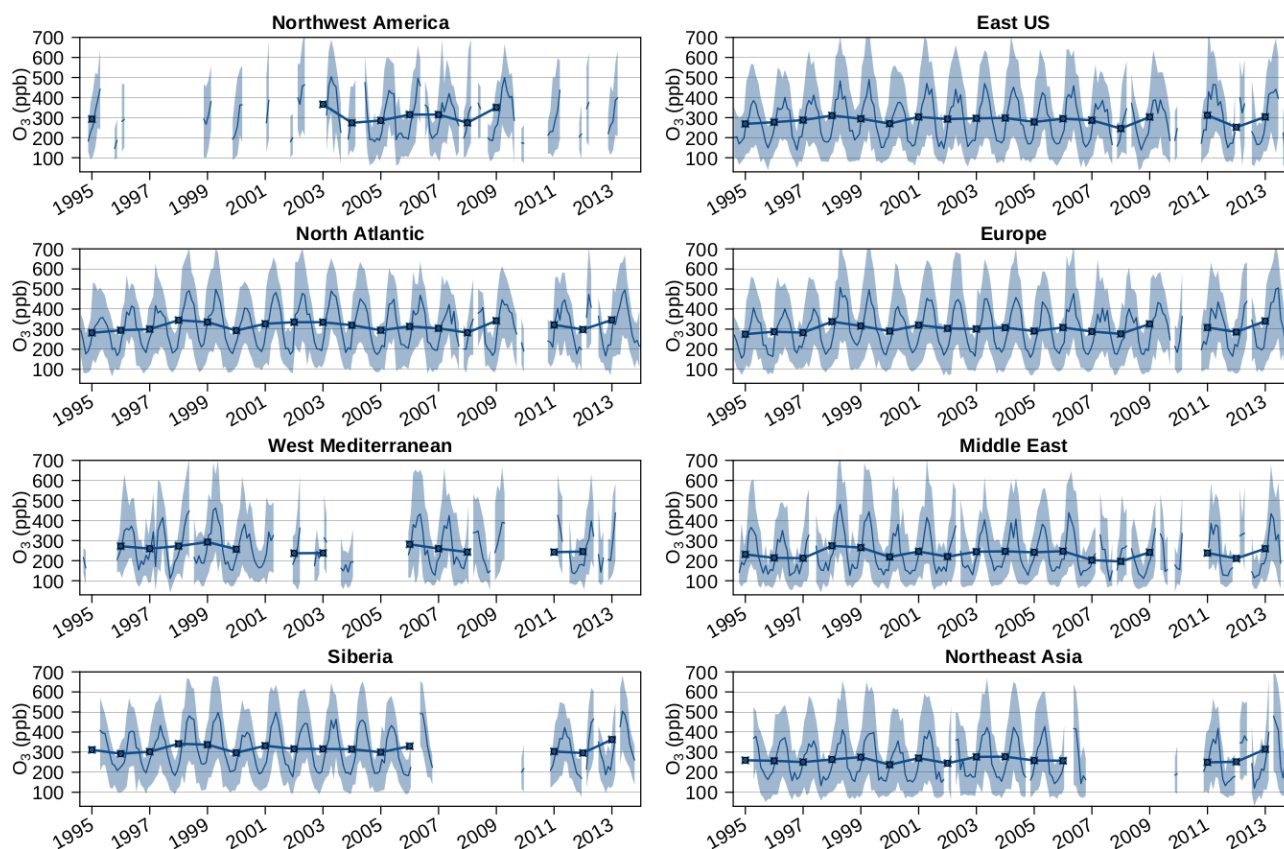
Figure 10. O$_3$ monthly mean values in the LS (thin curve). The interval from fifth and 95th percentiles is filled in blue. The yearly mean values are represented by the bold curve and the black points.

Upper tropospheric CO
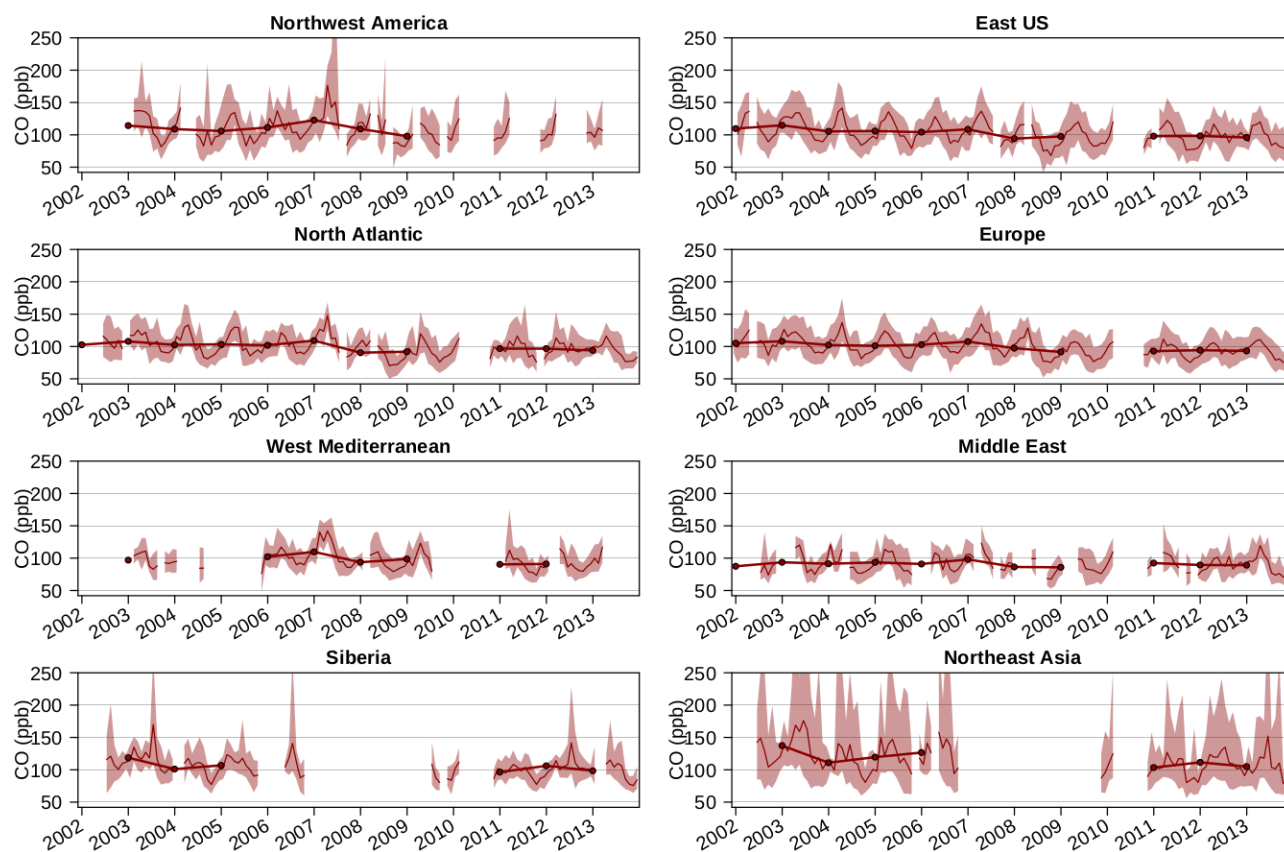
Figure 11. CO monthly mean values in the UT (thin curve). The interval from fifth and 95th percentiles is filled in red. The yearly mean values are represented by the bold curve and the black points.

Tropopause layer CO
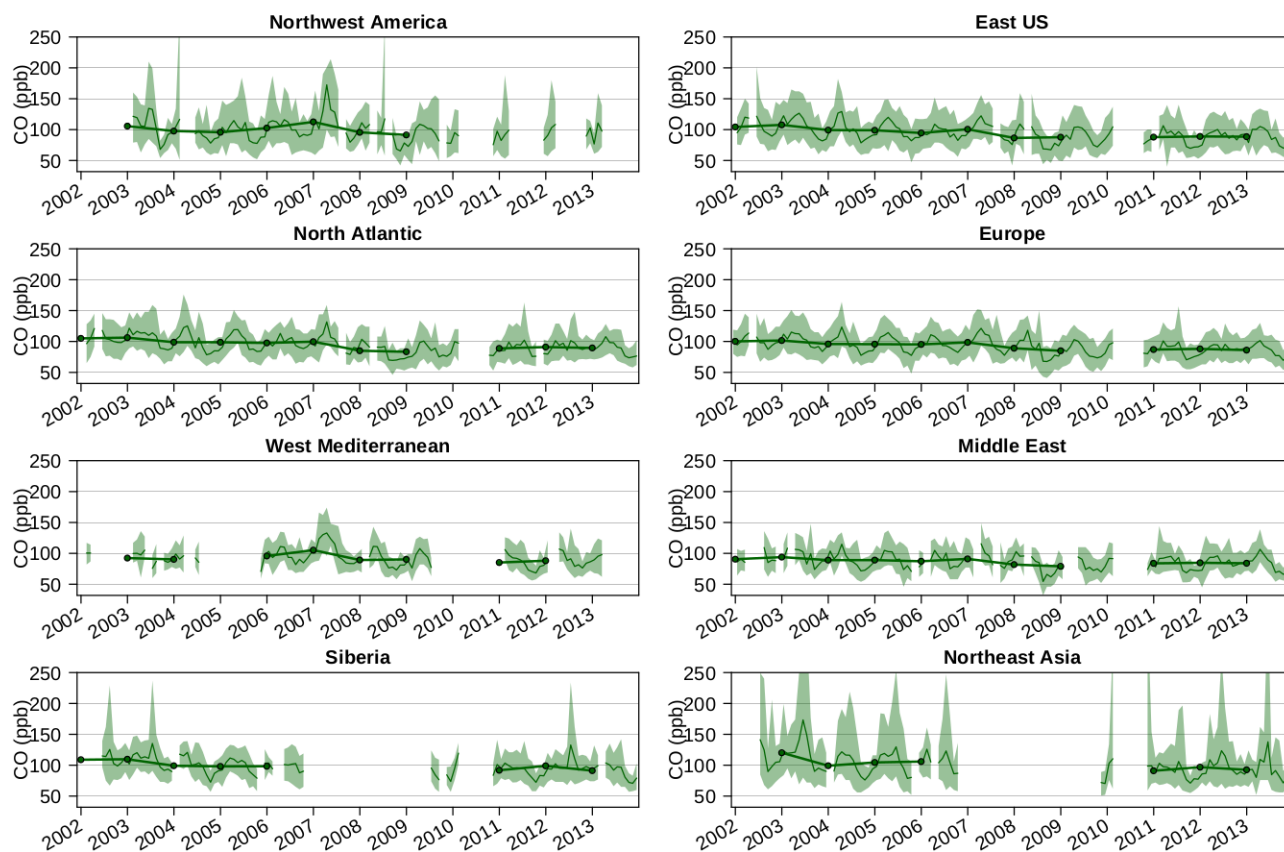
Figure 12. CO monthly mean values in the TPL (thin curve). The interval from fifth and 95th percentiles is filled in green. The yearly mean values are represented by the bold curve and the black points.

Lower stratospheric CO
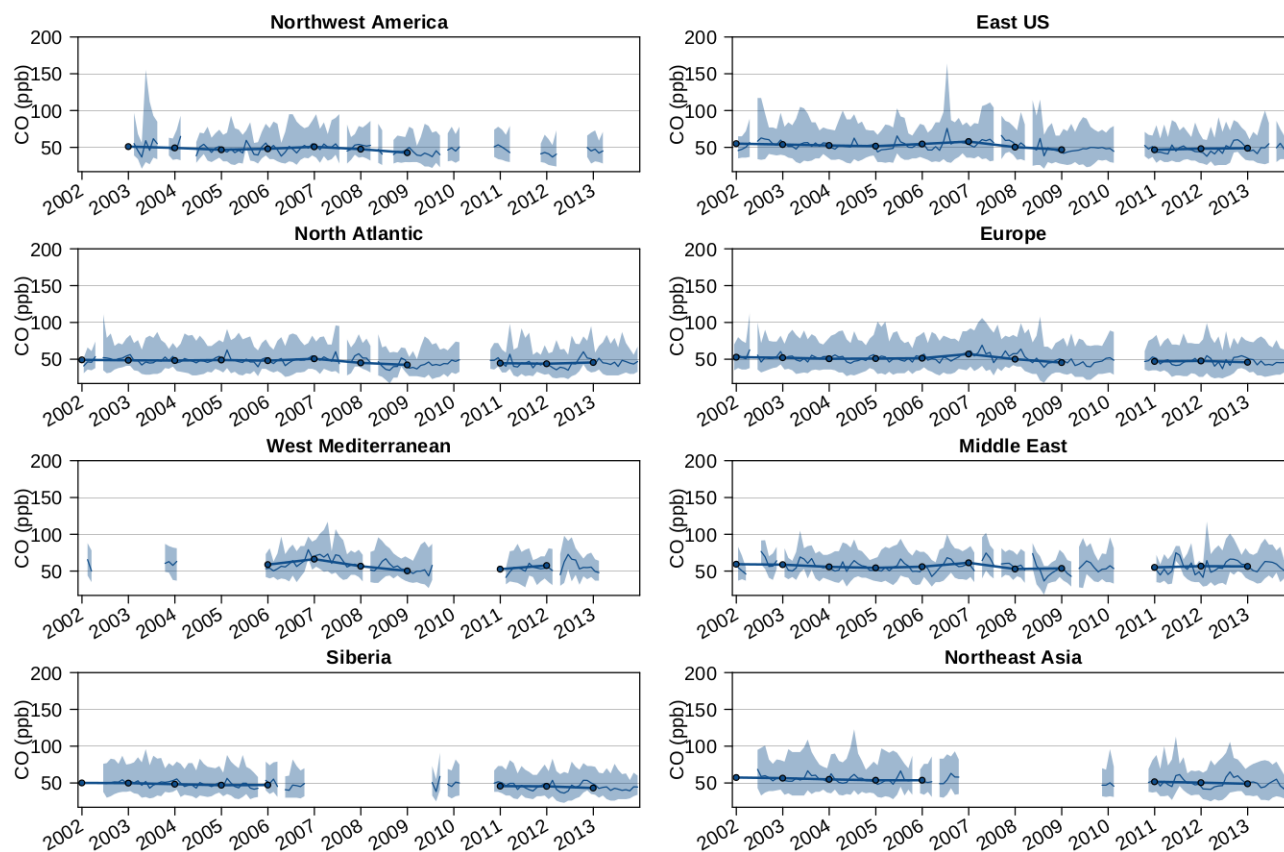
Figure 13. CO monthly mean values in the LS (thin curve). The interval from fifth and 95th percentiles is filled in blue. The yearly mean values are represented by the bold curve and the black points.

As it can be seen, no monthly data is available during most of 2010, due to an interruption of measurements.
Most regions have a good sampling efficiency, with about 70-97% of available data (see Tab. 1). Specifically, the lower sampling frequency in WNAm (top-left panel) allows relative few available monthly data. For O_3, the sampling focuses on the period 2003-2009. Since less than 60% of monthly data are available, and since the available months are especially representative

5   of the second half of the monitoring period, we cannot take it into account in the study of the 20-year trends. After 2009, the sampling is efficient only during winter, such that we can only compute the trend of wintertime CO in this region. The sampling is also too low for CO in WMed, in the LS (55%). In Siberia, Northeast Asia and WMed (excluding the LS for this region), the sampling is moderate for CO (between 60 and 70%) but data are available both at the beginning and at the end of period, which makes trend calculations still relevant.

10 For additional information, the monthly relative anomalies we used for the calculation of the trends are shown in Figs. A1 – A4.

In the UT, the anomalies have several common features: a negative anomaly until 1997, followed by a leveling off (2000 – 2009) and by a positive anomaly since 2011. The first period (1994-1997) has already been associated with the multi-year ozone recovery since the eruption of Mt Pinatubo in 1991: this event has been an important source of particulate matter in the lower stratosphere at global scale, contributing to the ozone depletion in the UT, TPL and LS (e.g. Tang et al., 2013). The

5   positive anomaly in 1998 has been referenced as a consequence of the extreme El Niño event in 1997, as explained in Thouret et al. (2006) and Koumoutsaris et al. (2008).

The LS does not show such a positive anomaly at the end of the period, nor the same IAV. We can note the positive anomalies in 2006 in WNAm, Eur and Sib. It seems consistent with the downward 380 K ozone flux anomalies shown in Olsen et al. (2013, Fig. 5).

10   ### 3.3.1   Trends in O_3

O_3 trends are summarized in Figs. 14 and 15. Figure 14 shows the trends of monthly fifth, mean values and 95th percentiles for O_3, on the left, central and right panels respectively. Figure 15 shows the trends of O_3 mean value in the UT, with respect to the seasons. In parallel, the absolute trends are reported in Tabs. B1 and B2 with their corresponding 95%-confidence intervals, in Appendix B. Note that all confidence intervals in this paper are given at the 95% level. For a better precision, we use the values

15   reported in this table to comment the following figures. The relative trends (in %.yr^{-1}) are also reported in Tabs. B3 and B4 in order to facilitate the comparison with other datasets. For clarity, only the significant trends at a 95% confidence level are reported.

At the annual scale, mean upper tropospheric O_3 is significantly increasing in the seven regions except NAt, with trend estimates ranging from +0.25 up to +0.45 ppb.yr^{-1}. The strongest and most significant trend is found in NEAs, with +0.45 [0.23; 0.68]

20   ppb.yr^{-1}. The least significant trend concerns the MidE region (+0.25 [0.01; 0.45] ppb.yr^{-1}). The trends in the TPL are similar to the upper tropospheric trends, albeit stronger and generally with a better significance. On the other hand, all mean O_3 trends remain insignificant in the LS.

Quite similar results are obtained for the O_3 fifth percentile in the UT and TPL. Again, the strongest increase in the UT is observed in NEAs (+0.57 [0.35; 0.80] ppb.yr^{-1}), closely followed by Sib (+0.50 [0.31; 0.67] ppb.yr^{-1}). The Atlantic regions

25   (EUS, NAt and Eur) exhibit an intermediate significance, with a stronger increase at approximately 0.45 ppb.yr^{-1} [0.20; 0.65] in EUS and NAt. The small southern regions (WMed and MidE) show the lowest and least significant increase at 0.34 [0.08; 0.52] and 0.30 [0.12; 0.48] ppb.yr^{-1} respectively. The main difference with the mean O_3 results is found in the LS where a significant positive trend is found in a few regions (North Atlantic, Siberia, Northeast Asia). On the other hand, the upper tropospheric P95 increases significantly in Eur and WMed only, at 0.29 [0.06; 0.47] ppb.yr^{-1} and 0.64 [0.06; 1.16] ppb.yr^{-1}

30   respectively, with p-values higher than 0.02 indicating a low significance level. In the TPL, the increase is observed in EUS, Eur and Sib, while no significant trend is found in the LS. Therefore, the general positive trend of mean O_3 mixing ratios in both the UT and TPL is associated with an increase of the background values (represented by the fifth percentile). WMed may be an exception with its strong increase of P95, contributing as well to the strong positive trend of the mean value.

The O_3 seasonal trends in the UT are shown in Fig. 15. As a main result, we note that each region shows a significant positive trend only during specific seasons. A significant increase of ∼0.5 ppb.yr^{-1} is observed in the Atlantic regions (EUS, NAt and Eur) in winter, with a non-negligible significance in NAt and Eur. Only Sib shows a significant increase during spring (0.50 ppb.yr^{-1}), as NEAs during summer (0.84 ppb.yr^{-1}). Most of the regions show a significant increase during fall. The fifth

5   percentile of O_3 mixing ratios is increasing in most regions during winter and spring. The strongest P05 trend is observed during summertime in NEAs (+1.07 [0.58; 1.42] ppb.yr^{-1}). Concerning the 95th percentile of O_3, all trends remain insignificant, except in Europe during winter (+0.43 [0.10; 0.88] ppb.yr^{-1}).

It is worth noting that besides the IAGOS database, in situ observations are very sparse in the UTLS and usually have a time

10   coverage which is too short for determining long-term trends. This considerably limits our ability to compare these results to the literature.

As mentionned in Sect. 1, the first 9 years of IAGOS measurements showed significant positive trends for ozone mixing ratios above eastern United States, northern Atlantic and Europe in the UT (respectively: +0.99 ± 0.82 %.yr^{-1}, +1.12 ± 0.86 %.yr^{-1} and +1.00 ± 0.90 %.yr^{-1}) and the LS (+1.54 ± 1.37 %.yr^{-1} above Northern Atlantic and +1.99 ± 1.21 %.yr^{-1} above Europe)

15   (Thouret et al., 2006). With a new decade of observations, our results suggest that the previous trends in the LS were influenced by the low values since 1994 until 1997, following Pinatubo's eruption.

More recently, Petetin et al. (2016) used IAGOS measurements to study vertical profiles of O_3 and CO above Frankfurt and Munich airports, during similar periods. As in Thouret et al. (2006), they defined the UT with the same method. In this layer, they found a barely significant increase of O_3 during winter. At the annual scale, they derived a significant positive trend of

20   P5, consistent with our results. However, they did not observe the significant positive trend of P95 that we derived. Since we compute the trends with the same methodology, the discrepancies are due to the greater size of our region Eur, which allows us a more frequent sampling, thus smoothing the temporal variability. We assume that in the UT, the spatial variability is too weak to be responsible for the discrepancies between the two studies.

25   In terms of O_3 trends in the free troposphere (rather than the UT), many studies highlighted increasing mixing ratios. Based on a combined data set (MOZAIC, research aircraft, ozonesondes, LiDAR) over western North America (25-55°N, 130-90°W), Cooper et al. (2010) derived an increase of springtime O_3 (April-May) in the UT over the period 1995-2008 (with trends of +0.58±0.52 ppb.yr^{-1} for the median O_3). Over the period 2000-2015, Granados-Muñoz and Leblanc (2016) derived a positive trend from LiDAR measurements above Table Mountain Facility (35°N, 119°W, Jet Propulsion Laboratory, California) at 7-10

30   km, with +0.31±0.30 ppb.yr^{-1} for the median (the trend of the 95th percentile being +0.55±0.60 ppb.yr^{-1}, thus insignificant at a 95% confidence level). Although no trend calculation was performed in WNAm, it may confirm the upper tropospheric O_3 increase as effective in the whole northern mid-latitudes, except the Pacific ocean. Based on ozonesondes over the period 1995-2008, Logan et al. (2012) did not observe any significant increase of O_3 mixing ratios between 400 and 300 hPa in Europe. The difference with our results may be partly explained by the fact that the period studied by Logan et al. (2012) does

35   not extent to 2011 when a strong positive O_3 anomaly in the UT is observed in the IAGOS data set (see Fig. 8).

Free and upper tropospheric ozone trends derived from various instruments were reviewed in Cooper et al. (2014). Significant positive trends over the period 1971 – 2010 are reported with ozonesonde data in the free troposphere above Western Europe and Japan, ranging at 0.1-0.3 ppb.yr^{-1}. As mentionned in section 1, the significant positive trends measured at the highest northern hemispheric GAW stations (above 2 km a.s.l.: Zugspitze, Rocky Mountain National Park, Jungfraujoch, Mt-Bachelor Observatory, Mt-Waliguan) rise between 0.05 ± 0.04 ppb.yr^{-1} and 0.33 ± 0.05 ppb.yr^{-1}. Only the most increasing trends (Rocky Mountain and Jungfraujoch) are within the range of the ones derived in the present study. Among the GAW stations mentionned in Sect. 1, the other ones show a smaller increase. In the free troposphere at 510 hPa, Neu et al. (2014a) derived a positive trend of $\simeq +1.1$ % yr^{-1} in the 30-50°N zonal band based on the Tropospheric Emission Spectrometer (TES) satellite measurements performed over the period 2005-2010, although on a shorter timescale. Thus, the increase of O$_3$ mixing ratio is likely to be more representative of the middle and upper altitude ranges of the free troposphere than its lower part. As said previously, the trends in the TPL are similar to the upper tropospheric ones. Since no lower stratospheric trend is significant at the annual scale, we cannot make any conclusion about the evolution of lower stratospheric ozone. Thus, our results alone do not allow us to explain these trends in the TPL. However, several studies reported a global significant increase of the tropopause height during the last decades (-0.05 hPa.yr^{-1}, $p < 2.10^{-16}$ over the period 1979-2011 with ERA-Interim reanalyses in Škerlak et al. (2014); see also Gettelman et al., 2011 and references therein). Above the regions of this study, the typical vertical gradient of O$_3$ observed in the 4 upper flight levels (thus the stronger part of the gradient) is about 1 ppb.hPa^{-1} (not shown). According to this yearly mean value, the elevation of the TPL would induce an ozone increase by an order of magnitude below the observed trends. Thus, such an increase of the TPL is not likely to explain a major part of the positive trends in the TPL.

Gettelman et al. (2010) combined a multimodel analysis to derive O$_3$ positive trends near 0.4%.yr^{-1} over the century in the extratropical UTLS (Ex-UTLS), relative to the tropopause. It is similar with the trends we derive in the UT, from 0.39%.yr^{-1} in MidE to 0.69%.yr^{-1} in NEAs (see Tab. B3). Their simulations did not show any dependence on tropospheric hydrocarbon chemistry. They concluded to an enhanced Brewer-Dobson circulation, which may subsequently contribute to the O$_3$ trends we observed in the UT and the TPL. This might explain the springtime positive trends we found in the TPL of NAt, Eur, Sib and NEAs, but these trends do not occur specifically during spring. Furthermore, only Sib shows a springtime significant increase in the UT.

The impact of the sampling density on the observed long-term evolution has been tested by computing the trends of the most 3 sampled regions with the time coverage of the lowest sampled regions. With the sampling periods of WMed and Sib, the changes for EUS, NAt and Eur were small compared to the confidence intervals (0.1%.yr^{-1} or less). With the sampling periods of NEAs, these trends tend to be higher, but the difference remains insignificant ($\simeq 0.2$%.yr^{-1}).
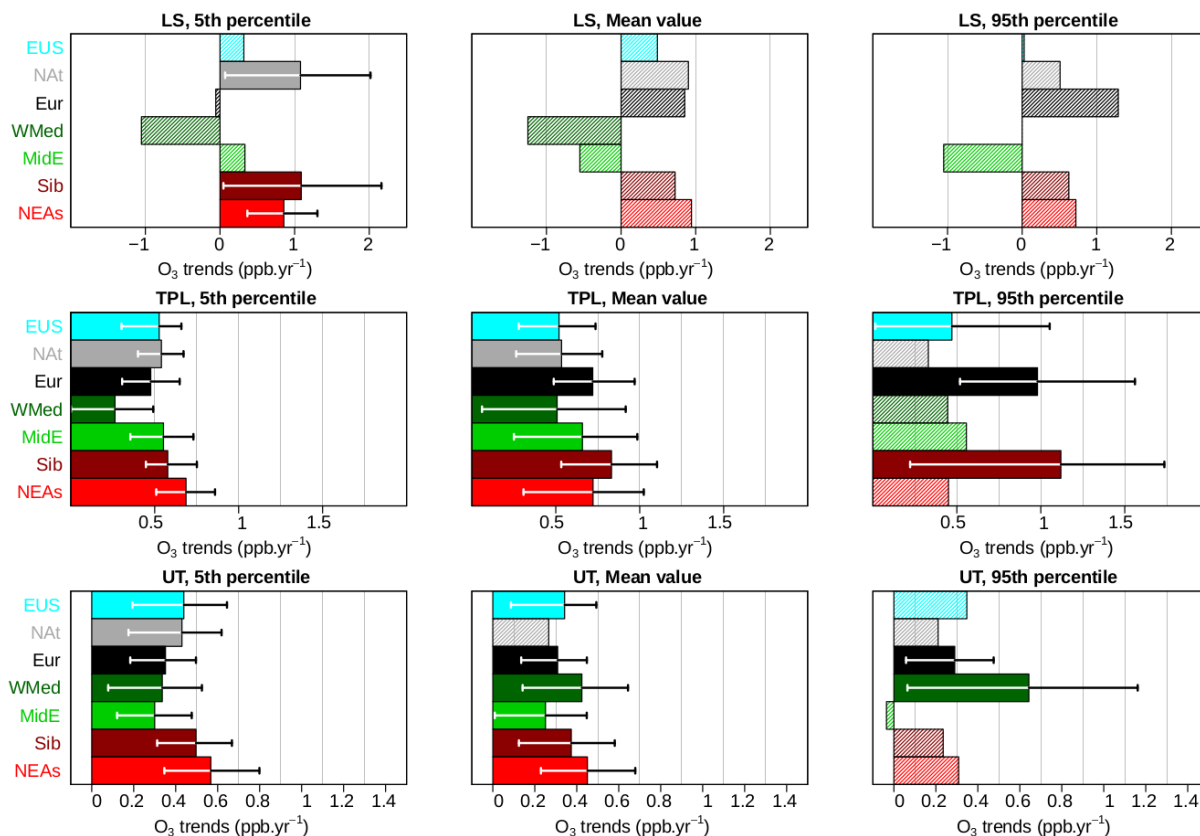
Figure 14. O_3 trends (ppb.yr^{-1}) in the UT, TPL and LS (from bottom to top), for the monthly fifth percentile (left panels), mean value (central panels) and 95th percentile (right panels). For each significant trend, the error bars represent the 95% confidence interval.
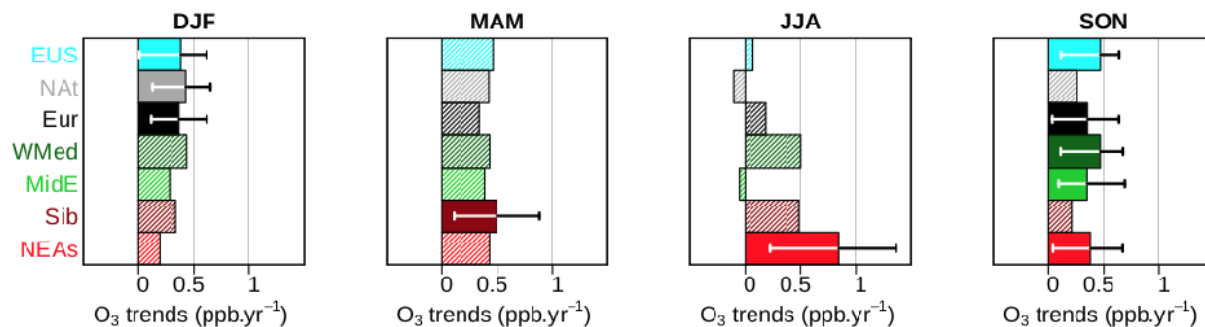
Figure 15. O_3 trends (ppb.yr^{-1}) in the UT, in each season. For each significant trend, the error bars represent the 95% confidence interval.

3.3.2 Trends in CO

CO trends are summarized in Figs. 16 and 17. As for O_3, more precise values are given in Tabs. B5 and B6 with their corresponding 95%-confidence intervals, followed by the equivalent relative trends in Tabs. B7 and B8, in the Appendix B. Figure 16 shows the trends of the fifth, mean values and 95th percentile for monthly CO data on the left, central and right panels respectively. Figure 17 shows the trends of CO mean value in the UT, with respect to the seasons. As discussed at the beginning of Sect. 3.3, we do not take the trend in the LS of WMed region into account. Similarly, only wintertime trends are taken into account in WNAm.

In all layers and almost all regions, the mean CO mixing ratios are significantly decreasing, with trends ranging between -0.80 and -2.19 ppb.yr^{-1} in the UT/TPL and between -0.5 and -0.8 ppb.yr^{-1} in the LS. The lowest and least significant trends are observed in the MidE region (significant only in the TPL, with -0.8 ppb.yr^{-1}). In the UT and TPL, the highest trends of mean CO are observed in the NEAs region (-2.19 [-3.33;-0.82] ppb.yr^{-1}). Results show a similar picture for the fifth percentile, although with usually slightly lower trends. Apart from the MidE region, these trends are well homogeneous among the different regions. The results appear more contrasted for the 95th percentile. In the UT, a strong negative trend is observed in NEAs (-3.81 [-6.75; -1.37] ppb.yr^{-1}), about a factor of 2 higher than the trends observed in EUS, NAt, Eur and Sib (about -1.9 ppb.yr^{-1}), while no significant trend is found in both WMed and MidE.

The main difference between 'northern and southern regions' lies in a higher magnitude and the significance of the P95 trends in the 5 'northern' regions (excluding WNAm, as mentionned previously). As discussed in the section 3.2, the two southern regions are expected to be less impacted by surface emissions, especially MidE because of a stronger subsidence. On the other hand, the CO decrease in the 5 'northern' regions is also influenced by the decrease of highest CO values (P95), i.e. less frequent and/or weaker high CO events. The strong interannual variability of P95 in NEAs is probably due to boreal forest fires.

Figure 17 shows the seasonal trends of upper tropospheric CO. The mean values decrease significantly in most regions during winter, from -1.15 [-3.67; -0.06] ppb.yr^{-1} in MidE to -2.97 [-5.00; -0.75] ppb.yr^{-1} in NEAs. During springtime, the negative trends persist in all regions but Sib and MidE. The summertime decrease is significant in EUS and Eur only, and the trends during fall are barely significant in Eur and WMed. Europe appears as the only region where negative mean CO trends are observed during all four seasons (although with a very low significance level during fall). The general decrease is also observed for both the fifth and 95th percentiles during all seasons except fall. The highest negative trends are usually observed in NEAs. However, due to a strong IAV, they are not always significant. For instance, albeit insignificant, a very strong negative trend of the 95th percentile of CO is observed in this region during springtime (-7.5 ppb.yr^{-1}). This decrease with its associated large uncertainties are likely linked to the decadal decrease of Asian boreal forest fires mentionned in Jiang et al. (2017).

The more homogeneous results obtained in winter compared to summer may be explained by a more efficient intercontinental transport of pollution. During winter, WCB events are more frequent and rather uplift the air masses with extrat-

ropical origins (Madonna et al., 2014). Consequently, this transport pathway may enhance the response of upper tropospheric CO mixing ratios to the reduction of surface emissions by a homogenized wintertime negative trend.

Most of our results in the UT over Europe are in agreement with the study of Petetin et al. (2016) based on IAGOS data above

5 Frankfurt and Munich airports, with similar CO negative trends. The main differences rely on an expected better significance for our trends, because of the size of Eur region allowing the use of a larger amount of data. It suggests the trends they derived in the UT above these airports are representative of the UT in Eur, and some of their insignificant trends are due to their limited amount of data, as they found insignificant trends in summer and autumn. They also found no significant trends for P5 during these seasons probably for the same reasons.

10 Over the whole troposphere, Worden et al. (2013) derived a global decrease of CO columns from MOPITT satellite observations over the period 2000-2011, with relative trends of -1.42±0.40 %.yr^{-1} in eastern US, -1.44±0.44 %.yr^{-1} in Europe and -1.60±0.96 %.yr^{-1} in eastern China. At the global scale, the decrease of CO columns observed by MOPITT over the period 2000-2012 is about -0.56 %.yr^{-1} (Laken and Shahbaz, 2014). In the northern hemisphere, the decrease of CO mixing ratio at 500 hPa observed by AIRS from 2003 to 2012 ranges between -1.28 ppb.yr^{-1} over lands and -1.01 ppb.yr^{-1} over oceans

15 (Worden et al., 2013). Using ground-based solar FTIR measurements at six European stations over the period 1998-2006, Angelbratt et al. (2011) observed similar negative trends of CO partial columns (0-15 km) in central/western Europe (around -1.2±0.2 %.yr^{-1} at Jungfraujoch and Zugspitze) and lower ones in northern Europe (about -0.6±0.2 %.yr^{-1} at Harestua, Norway and Kiruna, Sweden). All these results remain consistent with the trends we found in the UT, although the mean estimate of our trend in NEAs is substantially higher (-1.89 [-2.87; -0.71] %.yr^{-1}, see Tab. B7 in the Supplement). Gratz et al.

20 (2015) analysed springtime surface observations at Mount-Bachelor Observatory (Oregon, 2743 m a.s.l.) during 2004-2013 and showed a decrease of -3.1±2.4 ppb.yr^{-1}. They associated it with the decrease of CO anthropogenic emissions in Europe, North America and China. The decrease is substantially higher than in our study, probably because it concerns the lower part of the free troposphere, which is moire sensitive to the reduction of surface emissions.

The influence of the sampling frequency on the trends has been tested for each layer, and each statistic by applying the

25 sampling frequency to the monthly time series of the most 3 sampled regions (EUS, NAt, Eur). The higher bias was obtained in the UT, for the mean values and the P5, with the sampling frequency of WMed and MidE. Applying the sampling frequency of these regions weakened the absolute CO trends of 0.2 ppb.yr^{-1}, which remains negligible.
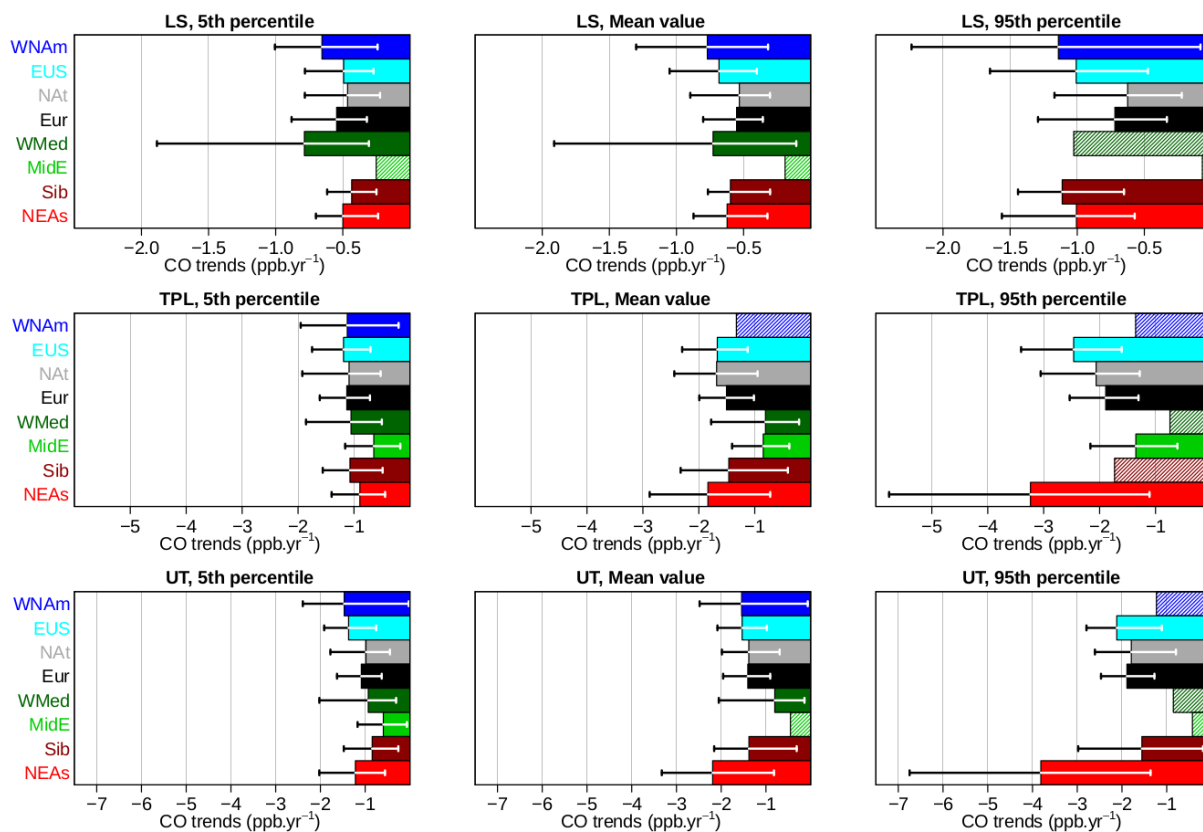
Figure 16. CO trends (ppb.yr^{-1}) in the UT, TPL and LS (from bottom to top), for the monthly fifth percentile (left panels), mean value (central panels) and 95th percentile (right panels). For each significant trend, the error bars represent the 95% confidence interval.
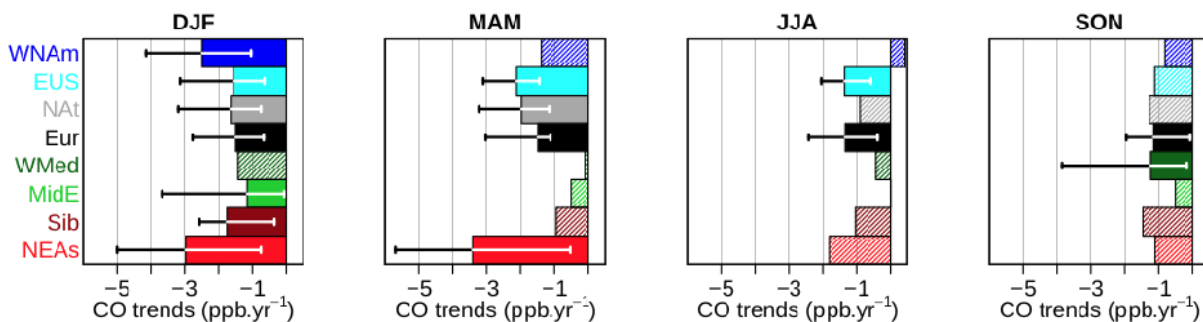
Figure 17. CO trends (ppb.yr^{-1}) in the UT, in each season. For each significant trend, the error bars represent the 95% confidence interval.

4 Summary and conclusions

In situ measurements in the UTLS are performed in the framework of the European research infrastructure IAGOS for ozone since 1994 and carbon monoxide since 2002. From IAGOS data, we have established a new global climatology for ozone and carbon monoxide in three different layers, the upper troposphere, tropopause layer and lower stratosphere over the periods August 1994 – December 2013 and December 2001 – December 2013, respectively. Thanks to its high frequency of measurements over long periods, the IAGOS database provides representative sets of data in the UTLS. In the present study, we examine more precisely the seasonal cycles and the (bi-) decadal trends of these trace gases, above eight subcontinental-scale regions of the northern extratropics. These regions cover a wide range of longitudes excluding so far the Pacific Ocean. For information, this latter region has been visited by IAGOS equipped aircraft since mid-2012. A first analysis of these data has been presented by Clark et al. (2015). One of the objectives of the present study was to highlight the regional variability in the UTLS in terms of horizontal composition distributions and trends. It is complementary with other analyses usually dealing with zonal means, and/or focusing on the vertical gradients of species. The methodology attributing air masses to UT, TPL and LS is the same as in Thouret et al. (2006). Added value to these previous results lies in a 10-year longer monitoring period above the major part of the extratropical northern hemisphere, completed with 12 years of CO measurements. As one of the major O_3 precursors at global scale, CO provides complementary information on the factors that control the O_3 seasonal cycles and trends.
The analysis of the horizontal mean seasonal distributions highlights the following general and regional characteristics:

- In the northern hemisphere, the more efficient photochemical activity is associated with the common summertime O_3 maximum in the UT, and the Brewer-Dobson circulation with the common springtime O_3 maximum in the LS. The general springtime CO maximum in the UT is seen as a consequence of the wintertime accumulation of emissions in the lower layers followed by an efficient vertical transport, before the summertime photochemical activity acts as a major sink for CO. However, CO maxima extend into summer over regions (and downwind regions) where large and intense boreal biomass burning occurs regularly, like Siberia and Canada. Another main feature of the northern hemisphere, in the UT, resides in a west-east difference of O_3 in summer with up to 15 ppb more over central Russia compared with eastern north America. There is also a systematic eastward gradient of CO from 60°E to 140°E of about 5 ppb by 10° longitude, especially noticeable in spring and summer.

- In the tropics, the CO mixing ratio maximizes in regions of biomass burning. Interestingly, the O_3 distribution presents the lowest mixing ratios for the four seasons on both sides of the Pacific Ocean. O_3 maximizes in SON over Southern Africa.

The mean O_3 seasonal cycles based on up to 19 years vary from 45 ppb in January to 80 ppb in June-July in the UT, and from 170 ppb in October-November to 400 ppb in April-May in the LS. The CO seasonal cycles based on 12 years data vary from 80 ppb in September-October to 120 in April in the UT, with a 140 ppb maximum in the two "Pacific regions" (Western North America and Northeast Asia). Most regions do not show any seasonal cycle in lower stratospheric CO. Comparing the mean seasonal cycles over these eight areas in the northern mid-latitudes highlights other regional characteristics like (i) a broad

spring-summer CO maximum over Northeast Asia (NEAs), and (ii) a springtime O_3 maximum over Western North America (WNAm) and Northeast Asia to a lesser extend. Such summertime irregularities in the upper tropospheric cycles of O_3 mixing ratios above the two "Pacific regions" likely highlight the impact of the Asian and North American monsoons, bringing poor-

5 O_3 air masses from the subtropical Pacific Ocean. Indeed, the springtime and summertime CO maxima in the UT suggest that WNAm and NEAs are located downwind of a common area with strong emissions (anthropogenic and biomass burning emissions). In the LS, the Middle-East region (MidE) shows the lowest O_3 and highest CO mixing ratios. This can be related to the impact of subtropical air masses uplifted in the Asian monsoon, then transported northward by the western branch of the anticyclonic circulation.

10 The bi-decacal trends in O_3 are positive and statistically significant at a 2σ level in most regions (excluding North Atlantic), with the best estimate of the trend ranging from +0.25 to +0.45 ppb.yr^{-1} on average. This evolution appears to be linked to the increase of the lowest values, and not necessarily with the highest values. Seasonal O_3 mixing ratios show a significant increase during fall and winter in the three Atlantic regions (Eastern US, North Atlantic and Europe), and a significant increase during spring or summer in the Asian regions, Siberia and Northeast Asia, respectively. Such a regional difference in the seasonality of

15 O_3 trends suggests that the increase in the Atlantic regions is linked to a long-term elevation of the background mixing ratios, while emissions of precursors during favorable photochemical conditions still drive part of the increase over Asia. The trends in O_3 in the TPL are similar to the trends in the UT, albeit stronger and generally with a better significance. Nevertheless, all mean O_3 trends remain insignificant in the LS. This is different from the results presented in Thouret et al. (2006), where the first nine years of IAGOS data showed positive trends in O_3 in the LS, with the same magnitude as those in the UT. With an

20 additional decade of observations, our present results suggest that the previous reported trends in the LS were influenced by the low values from 1994 until 1997 and the 1998-1999 positive anomaly, i.e. during the O_3 recovery after Pinatubo's eruption in 1991, followed by the global anomaly subsequent to the extreme El-Niño event of 1997 (Koumoutsaris et al., 2008).

The decadal trends in CO are negative and significant in most regions (excluding MidE), with the best estimate ranging from -1.5 to -2.2 ppb.yr^{-1} on average in the UT. Both fifth and 95th percentiles from the CO distribution are decreasing. The

25 decrease in the lowest values is more homogeneous than in the highest values, which can be related to the strong interannual variability of biomass burning emissions. However, the wintertime decrease is significant in the UT over all regions, while the summertime trends are either very low or not significant. The strongest decreases are observed in winter and spring over NEAs. As the overall decrease is associated with the reduction of surface emissions in the northern extratropics, the locally insignificant trends of P95 above MidE suggests that the UT over there is less impacted by surface emissions than over other

30 regions. This was indeed the rationale for defining this region as the "large scale subsidence" region.

Negative trends in CO in the UT definitely show the impact of global reduction of surface emissions. Positive trends in O_3 in the UT and TPL definitely show no direct link between the long-term evolution of O_3 and surface CO emissions. It is important to note that CO does not represent all the O_3 precursors. Trends in the LS are not significant for O_3 over this period. Therefore, it is still difficult to attribute the trends of O_3 in the UT to one leading process. The lowest trends in both O_3 and

35 CO in the MidE region, where the UT is less influenced by the middle and lower troposphere, may reflect a significant global tropospheric contribution driving the higher trends of O_3 and CO over other regions. This is in line with recent findings by

Zhang et al. (2016), attributing the major part of the increase in the northern hemisphere tropospheric O_3 burden to the increase in the emissions located between the tropics. However, the increase in the O_3 mixing ratio takes place in almost every region, and the regional differences are not statistically significant to exclude other leading processes. We compared our results to other

5   studies analyzing trends in lower tropospheric levels. It is clear that the O_3 increases observed in most free tropospheric GAW stations are weaker than the ones in the middle and upper troposphere. This difference between the upper sublayers and the lower one in the free troposphere is found notably in Tanimoto et al. (2017, in preparation) using aircraft, sondes and surface measurements in Japan from 1991 to 2015. On one hand, the O_3 mixing ratios were shown to increase monotonically in the middle and upper parts of the free troposphere. On the other hand, the lower part of the free troposphere was characterized by

10   an increase until 2000, then by a flattening. They concluded that it was linked to the influence of the decreasing baseline O_3 in the boundary layer. It may suggest that the O_3 trends in the UT are further linked to in situ emissions of precursors directly in the UT (lightning, aircraft) and/or an increase in the mid-latitudinal STE O_3 flux as reported in other studies (e.g. Neu et al., 2014a). The latter is not inconsistent with our results in the LS, as the absence of a significant trend of O_3 in this layer may be due to a strong IAV. It is also consistent with the increase in O_3 STE over the century suggested by Neu et al. (2014a), and the

15   increase in the vertical STT mass flux in the extratropics during 1996-2011 modeled with ERA-Interim and JRA-55 reanalyses (Boothe and Homeyer, 2017), linked to the acceleration of the Brewer-Dobson circulation, in agreement with observations and chemistry-climate models (Butchart, 2014 and references therein; more recently, e.g. Garfinkel et al., 2017).

Finally, IAGOS data have shown significant regional and interannual variabilities that can provide helpful information for shorter and/or localized observation campaigns. The vertical accuracy makes IAGOS an available tool for realistic comparisons

20   with CTMs and CCMs, allowing a precise evaluation of their ability to reproduce characteristics of the chemical composition of the UTLS, including climatologies and trends.

5   Data availability

All ozone and carbon monoxide data sets used in this study were obtained from the existing IAGOS, freely available on the IAGOS website (http://www.iagos.org) and via the AERIS website (http://www.aeris-data.fr).

25   *Acknowledgements.* The authors acknowledge the strong support of the European Commission, Airbus, and the Airlines (Lufthansa, Air-France, Austrian, Air Namibia, Cathay Pacific, Iberia and China Airlines so far) who carry the MOZAIC or IAGOS equipment and perform the maintenance since 1994. In its last 10 years of operation, MOZAIC has been funded by INSU-CNRS (France), Météo-France, Université Paul Sabatier (Toulouse, France) and Research Center Jülich (FZJ, Jülich, Germany). IAGOS has been additionally funded by the EU projects IAGOS-DS and IAGOS-ERI. The MOZAIC-IAGOS database is supported by AERIS (CNES and INSU-CNRS). Data are also available via

30   AERIS web site www.aeris-data.fr. The authors ought to thank the Midi-Pyrénées region and Météo-France too, for funding Yann Cohen's PhD.

Appendix A: Monthly anomalies

Upper tropospheric O$_3$
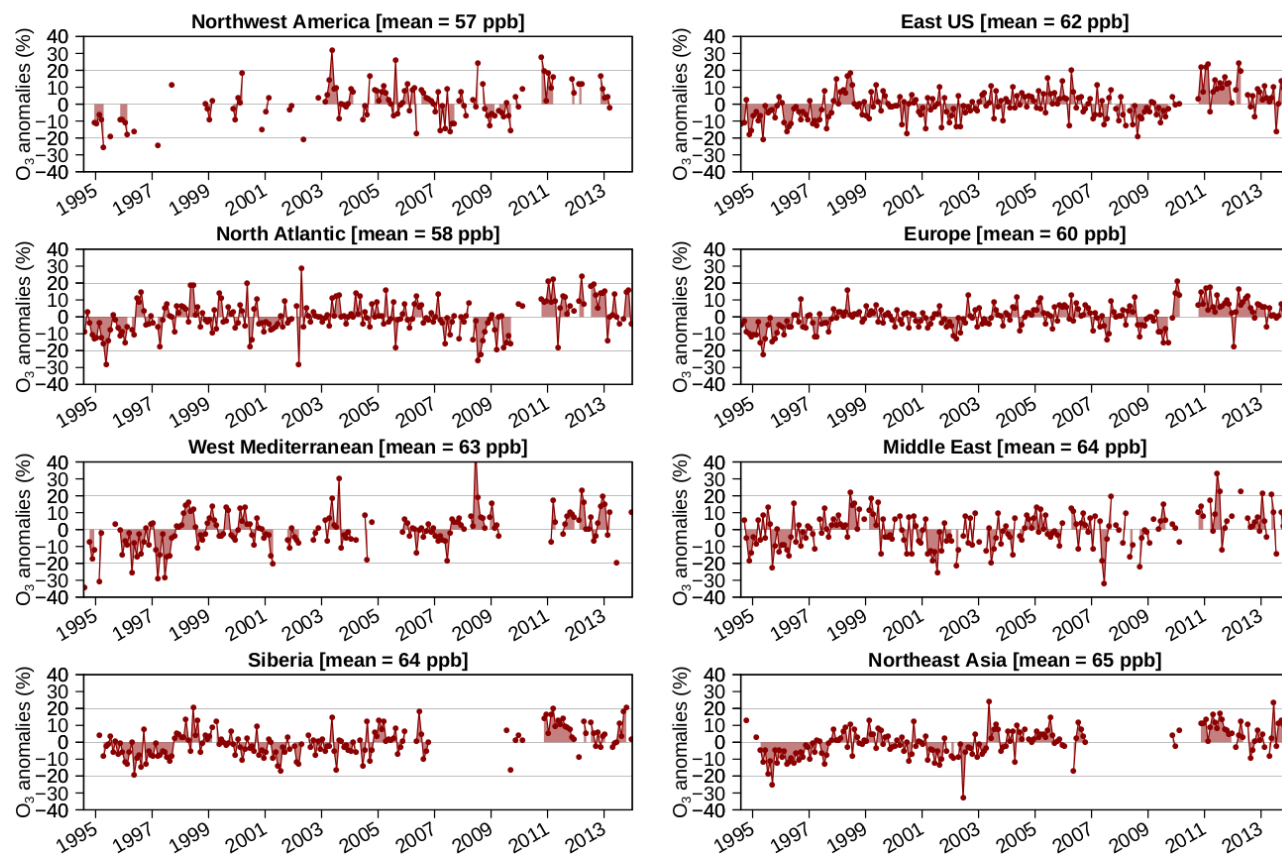
Figure A1. Relative monthly anomalies of O$_3$ volume mixing ratio in the upper troposphere. The units % refer to the corresponding climatological means indicated above each graphic.

Lower stratospheric O₃
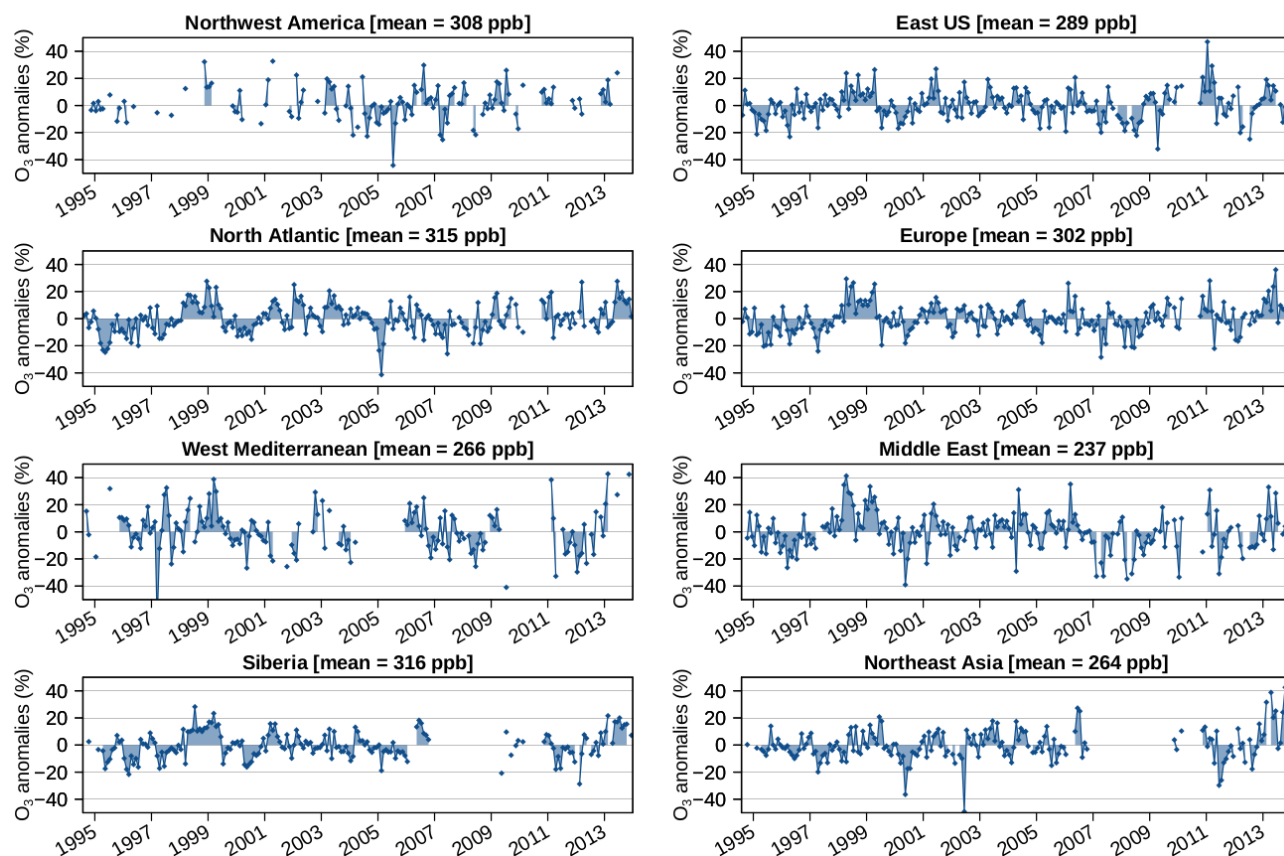
Figure A2. Relative monthly anomalies of O₃ volume mixing ratio in the lower stratosphere. The units % refer to the corresponding climatological means indicated above each graphic.

Upper tropospheric CO
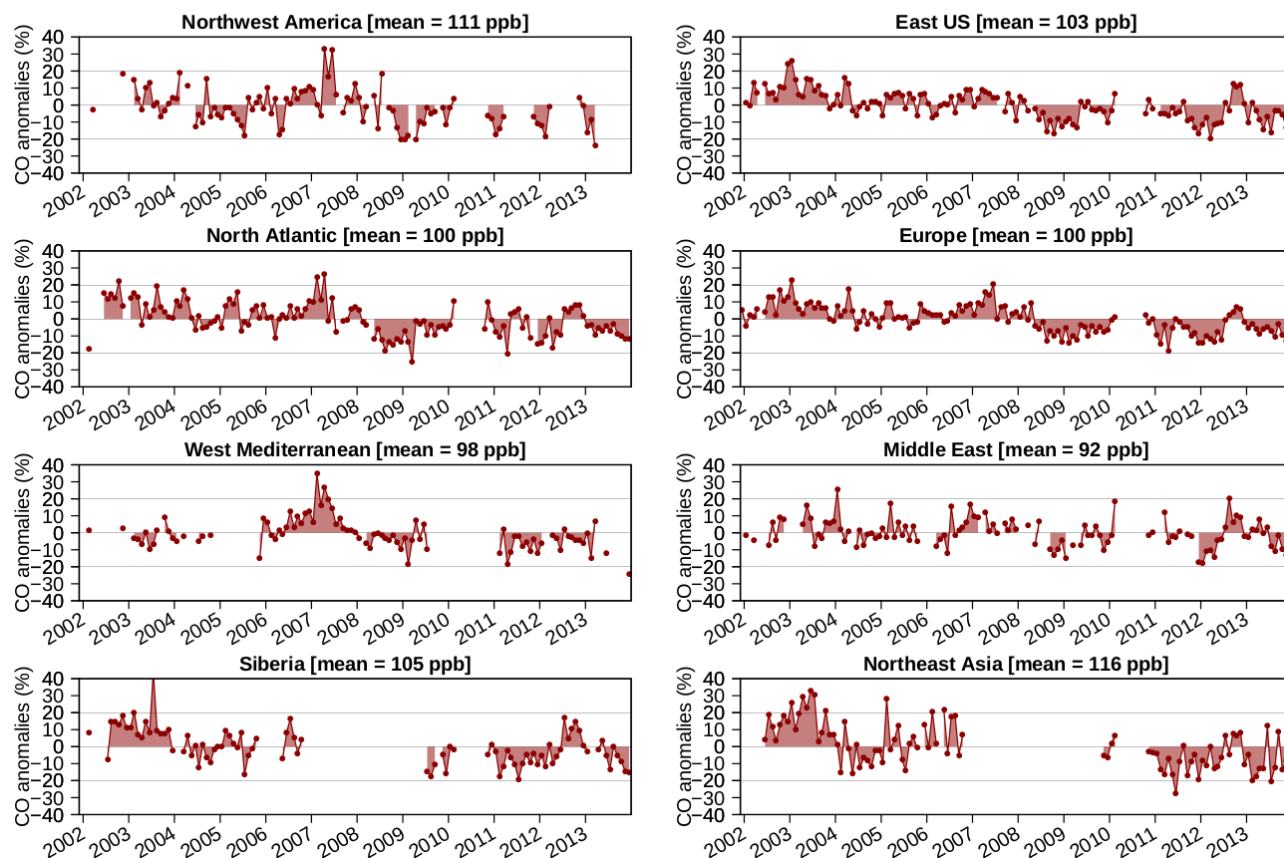
Figure A3. Relative monthly anomalies of CO volume mixing ratio in the upper troposphere. The units % refer to the corresponding climatological means indicated above each graphic.

Lower stratospheric CO
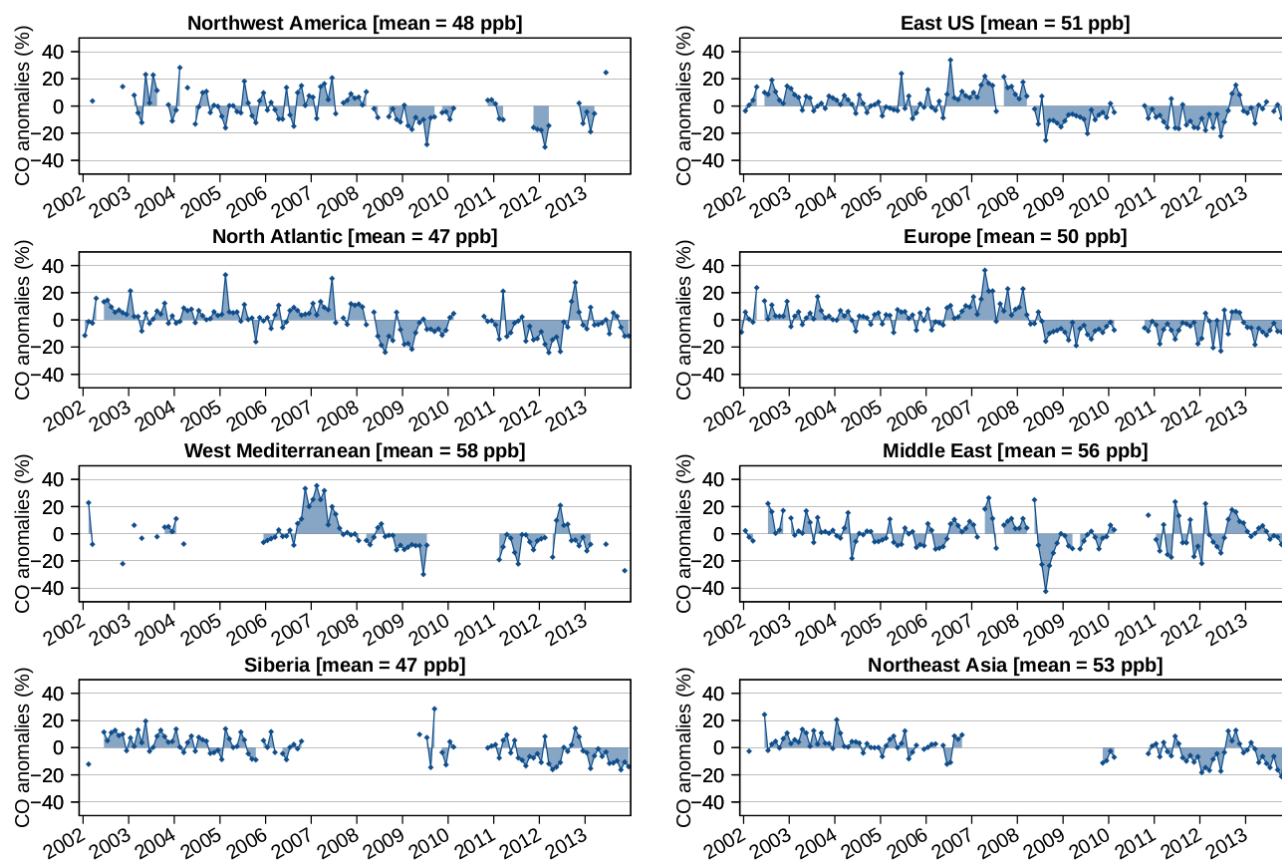
Figure A4. Relative monthly anomalies of CO volume mixing ratio in the lower stratosphere. The units % refer to the corresponding climatological means indicated above each graphic.

Appendix B: Tables of trends

Table B1. O_3 absolute trends in ppb.yr^{-1} during all the year in the UT. From left to right, the anomalies are taken from deseasonalised P05, monthly means and P95. The insignificant trends with respect to the 95 % confidence level are indicated as NS.

SEASON	REGION		P05			MEAN			P95	
(ppb.yr^{-1})		Slope	Conf. int. (95%)	p-value	Slope	Conf. int. (95%)	p-value	Slope	Conf. int. (95%)	p-value
ANN	EUS	0.44	[0.19;0.64]	0.003	0.34	[0.09;0.50]	0.013		NS	
	NAt	0.43	[0.18;0.62]	0.003		NS			NS	
	Eur	0.35	[0.18;0.50]	$<10^{-3}$	0.31	[0.14;0.45]	0.003	0.29	[0.06;0.47]	0.022
	WMed	0.34	[0.08;0.52]	0.003	0.42	[0.14;0.64]	0.003	0.64	[0.06;1.16]	0.04
	MidE	0.30	[0.12;0.48]	0.007	0.25	[0.01;0.45]	0.037		NS	
	Sib	0.50	[0.31;0.67]	$<10^{-3}$	0.37	[0.12;0.58]	0.007		NS	
	NEAs	0.57	[0.35;0.80]	$<10^{-3}$	0.45	[0.23;0.68]	$<10^{-3}$		NS	

Table B2. O_3 absolute trends in ppb.yr^{-1} during all the year during each season in the UT. From left to right, the anomalies are taken from deseasonalised P05, monthly means and P95. The insignificant trends with respect to the 95 % confidence level are indicated as NS.

SEASON (ppb.yr^{-1})	REGION	P05 Slope	P05 Conf. int. (95%)	P05 p-value	MEAN Slope	MEAN Conf. int. (95%)	MEAN p-value	P95 Slope	P95 Conf. int. (95%)	P95 p-value
DJF	EUS	0.50	[0.16;0.93]	0.007	0.38	[0.01;0.61]	0.04		NS	
	NAt	0.54	[0.34;0.84]	$<10^{-3}$	0.43	[0.13;0.65]	0.003		NS	
	Eur	0.41	[0.13;0.72]	$<10^{-3}$	0.37	[0.11;0.62]	0.003	0.43	[0.10;0.88]	0.008
	WMed		NS			NS			NS	
	MidE		NS			NS			NS	
	Sib	0.50	[0.11;0.91]	0.02		NS			NS	
	NEAs	0.34	[0.12;0.76]	0.003		NS			NS	
MAM	EUS		NS			NS			NS	
	NAt	0.63	[0.09;1.03]	0.028		NS			NS	
	Eur		NS			NS			NS	
	WMed	0.53	[0.10;1.11]	0.037		NS			NS	
	MidE	0.48	[0.15;1.00]	0.017		NS			NS	
	Sib	0.56	[0.24;1.00]	0.018	0.50	[0.11;0.88]	0.023		NS	
	NEAs	0.56	[0.17;0.82]	0.007		NS			NS	
JJA	EUS		NS			NS			NS	
	NAt		NS			NS			NS	
	Eur		NS			NS			NS	
	WMed		NS			NS			NS	
	MidE		NS			NS			NS	
	Sib	0.60	[0.42;0.91]	$<10^{-3}$		NS			NS	
	NEAs	1.07	[0.58;1.42]	0.003	0.84	[0.23;1.36]	0.01		NS	
SON	EUS	0.44	[0.05;0.76]	0.012	0.47	[0.11;0.64]	0.013		NS	
	NAt		NS			NS			NS	
	Eur	0.40	[0.00;0.64]	0.045	0.35	[0.04;0.64]	0.033		NS	
	WMed	0.38	[0.16;0.54]	0.003	0.47	[0.11;0.67]	0.02		NS	
	MidE	0.26	[0.05;0.52]	0.023	0.35	[0.09;0.69]	0.01		NS	
	Sib		NS			NS			NS	
	NEAs		NS		0.38	[0.04;0.67]	0.043		NS	

Table B3. O_3 relative trends in %.yr^{-1} during all the year in the UT. From left to right, the anomalies are taken from deseasonalised P05, monthly means and P95. The insignificant trends with respect to the 95 % confidence level are indicated as NS.

SEASON	REGION	P05			MEAN			P95		
(%.yr^{-1})		Slope	Conf. int. (95%)	p-value	Slope	Conf. int. (95%)	p-value	Slope	Conf. int. (95%)	p-value
ANN	EUS	1.10	[0.48;1.61]	0.003	0.55	[0.14;0.80]	0.013		NS	
	NAt	1.10	[0.45;1.59]	0.003		NS			NS	
	Eur	0.88	[0.46;1.24]	$<10^{-3}$	0.51	[0.23;0.75]	0.003	0.33	[0.07;0.53]	0.022
	WMed	0.82	[0.19;1.28]	0.003	0.67	[0.23;1.02]	0.003	0.70	[0.07;1.26]	0.04
	MidE	0.68	[0.27;1.08]	0.007	0.39	[0.01;0.70]	0.037		NS	
	Sib	1.06	[0.66;1.42]	$<10^{-3}$	0.58	[0.19;0.91]	0.007		NS	
	NEAs	1.26	[0.77;1.78]	$<10^{-3}$	0.69	[0.35;1.04]	$<10^{-3}$		NS	

Table B4. O_3 relative trends in %.yr^{-1} during each season in the UT. From left to right, the anomalies are taken from deseasonalised P05, monthly means and P95. The insignificant trends with respect to the 95 % confidence level are indicated as NS.

SEASON ($\%.yr^{-1}$)	REGION	P05 Slope	P05 Conf. int. (95%)	P05 p-value	MEAN Slope	MEAN Conf. int. (95%)	MEAN p-value	P95 Slope	P95 Conf. int. (95%)	P95 p-value
DJF	EUS	1.24	[0.39;2.32]	0.007	0.62	[0.01;0.99]	0.04		NS	
	NAt	1.38	[0.87;2.16]	$<10^{-3}$	0.74	[0.22;1.12]	0.003		NS	
	Eur	1.02	[0.33;1.79]	$<10^{-3}$	0.61	[0.19;1.03]	0.003	0.48	[0.11;0.99]	0.008
	WMed		NS			NS			NS	
	MidE		NS			NS			NS	
	Sib	1.07	[0.23;1.93]	0.02		NS			NS	
	NEAs	0.75	[0.27;1.70]	0.003		NS			NS	
MAM	EUS		NS			NS			NS	
	NAt	1.61	[0.22;2.63]	0.028		NS			NS	
	Eur		NS			NS			NS	
	WMed	1.30	[0.25;2.71]	0.037		NS			NS	
	MidE	1.10	[0.34;2.27]	0.017		NS			NS	
	Sib	1.20	[0.50;2.13]	0.018	0.78	[0.17;1.38]	0.023		NS	
	NEAs	1.24	[0.37;1.83]	0.007		NS			NS	
JJA	EUS		NS			NS			NS	
	NAt		NS			NS			NS	
	Eur		NS			NS			NS	
	WMed		NS			NS			NS	
	MidE		NS			NS			NS	
	Sib	1.28	[0.90;1.93]	$<10^{-3}$		NS			NS	
	NEAs	2.37	[1.29;3.15]	0.003	1.30	[0.35;2.10]	0.01		NS	
SON	EUS	1.10	[0.12;1.91]	0.012	0.76	[0.18;1.03]	0.013		NS	
	NAt		NS			NS			NS	
	Eur	1.00	[0.00;1.60]	0.045	0.59	[0.06;1.06]	0.033		NS	
	WMed	0.92	[0.38;1.31]	0.003	0.74	[0.17;1.07]	0.02		NS	
	MidE	0.60	[0.12;1.19]	0.023	0.55	[0.14;1.08]	0.01		NS	
	Sib		NS			NS			NS	
	NEAs		NS		0.58	[0.06;1.03]	0.043		NS	

Table B5. CO absolute trends in ppb.yr^{-1} during all the year in the UT. From left to right, the anomalies are taken from deseasonalised P05, monthly means and P95. The insignificant trends with respect to the 95 % confidence level are indicated as NS.

SEASON	REGION	P05			MEAN			P95		
(ppb.yr^{-1})		Slope	Conf. int. (95%)	p-value	Slope	Conf. int. (95%)	p-value	Slope	Conf. int. (95%)	p-value
ANN	EUS	-1.37	[-1.92;-0.75]	<10^{-3}	-1.53	[-2.08;-0.98]	<10^{-3}	-2.12	[-2.80;-1.10]	<10^{-3}
	NAt	-0.98	[-1.77;-0.45]	0.003	-1.38	[-1.98;-0.69]	<10^{-3}	-1.79	[-2.61;-0.79]	<10^{-3}
	Eur	-1.08	[-1.63;-0.63]	<10^{-3}	-1.41	[-1.96;-0.90]	<10^{-3}	-1.89	[-2.47;-1.28]	<10^{-3}
	WMed	-0.93	[-2.02;-0.31]	0.003	-0.80	[-2.06;-0.14]	0.013		NS	
	MidE	-0.59	[-1.17;-0.07]	0.027		NS			NS	
	Sib	-0.84	[-1.48;-0.26]	0.007	-1.38	[-2.15;-0.32]	0.01	-1.56	[-2.98;-0.19]	0.02
	NEAs	-1.22	[-2.02;-0.56]	<10^{-3}	-2.19	[-3.33;-0.82]	0.003	-3.81	[-6.75;-1.37]	0.003

Table B6. CO absolute trends in $ppb.yr^{-1}$ during each season in the UT. From left to right, the anomalies are taken from deseasonalised P05, monthly means and P95. The insignificant trends with respect to the 95 % confidence level are indicated as NS. Note that the trends in WNAm are available only in DJF.

SEASON	REGION	P05			MEAN			P95		
($ppb.yr^{-1}$)		Slope	Conf. int. (95%)	p-value	Slope	Conf. int. (95%)	p-value	Slope	Conf. int. (95%)	p-value
DJF	WNAm		NS		-2.48	[-4.14;-1.04]	0.02	-3.30	[-6.25;-1.12]	0.003
	EUS		NS		-1.56	[-3.13;-0.65]	$<10^{-3}$	-2.42	[-3.42;-1.42]	$<10^{-3}$
	NAt		NS		-1.65	[-3.19;-0.75]	0.007	-2.68	[-4.21;-1.46]	0.005
	Eur	-1.24	[-2.32;-0.37]	0.01	-1.49	[-2.77;-0.67]	0.007	-2.15	[-3.54;-1.19]	0.007
	WMed		NS			NS			NS	
	MidE		NS		-1.15	[-3.67;-0.06]	0.05		NS	
	Sib	-0.99	[-2.24;-0.15]	0.035	-1.75	[-2.56;-0.35]	0.023	-1.43	[-3.24;-0.39]	0.025
	NEAs	-2.51	[-3.32;-1.55]	$<10^{-3}$	-2.97	[-5.00;-0.75]	0.01		NS	
MAM	EUS	-1.92	[-3.03;-1.00]	$<10^{-3}$	-2.11	[-3.10;-1.45]	$<10^{-3}$	-2.66	[-3.86;-0.99]	0.017
	NAt	-1.88	[-3.81;-0.79]	0.013	-1.97	[-3.24;-1.16]	0.003		NS	
	Eur	-1.19	[-2.42;-0.26]	0.017	-1.49	[-3.03;-1.12]	0.003	-2.03	[-3.69;-1.51]	0.003
	WMed		NS			NS			NS	
	MidE		NS			NS			NS	
	Sib		NS			NS			NS	
	NEAs	-1.54	[-2.55;-0.02]	0.05	-3.42	[-5.70;-0.53]	0.03		NS	
JJA	EUS	-1.39	[-2.09;-0.85]	$<10^{-3}$	-1.36	[-2.05;-0.58]	0.003	-1.88	[-3.38;-0.34]	0.007
	NAt		NS			NS			NS	
	Eur	-1.01	[-1.99;-0.42]	0.007	-1.34	[-2.41;-0.38]	0.01	-1.80	[-2.99;-0.50]	0.017
	WMed		NS			NS			NS	
	MidE		NS			NS			NS	
	Sib		NS			NS			NS	
	NEAs		NS			NS			NS	
SON	EUS		NS			NS			NS	
	NAt		NS			NS			NS	
	Eur		NS		-1.14	[-1.96;-0.07]	0.023		NS	
	WMed		NS		-1.23	[-3.85;-0.17]	0.04	-1.29	[-5.70;-0.40]	0.018
	MidE		NS			NS			NS	
	Sib		NS			NS			NS	
	NEAs		NS			NS			NS	

Table B7. CO relative trends in $\%.yr^{-1}$ during all the year, and during each season in the UT. From left to right, the anomalies are taken from deseasonalised P05, monthly means and P95. The insignificant trends with respect to the 95 % confidence level are indicated as NS.

SEASON	REGION	P05			MEAN			P95		
$(\%.yr^{-1})$		Slope	Conf. int. (95%)	p-value	Slope	Conf. int. (95%)	p-value	Slope	Conf. int. (95%)	p-value
ANN	EUS	-1.74	[-2.43;-0.95]	$<10^{-3}$	-1.49	[-2.02;-0.95]	$<10^{-3}$	-1.63	[-2.15;-0.85]	$<10^{-3}$
	NAt	-1.21	[-2.19;-0.55]	0.003	-1.38	[-1.98;-0.69]	$<10^{-3}$	-1.47	[-2.14;-0.65]	$<10^{-3}$
	Eur	-1.39	[-2.09;-0.81]	$<10^{-3}$	-1.41	[-1.96;-0.90]	$<10^{-3}$	-1.54	[-2.01;-1.04]	$<10^{-3}$
	WMed	-1.15	[-2.50;-0.38]	0.003	-0.82	[-2.10;-0.14]	0.013		NS	
	MidE	-0.80	[-1.58;-0.09]	0.027		NS			NS	
	Sib	-0.99	[-1.74;-0.30]	0.007	-1.31	[-2.05;-0.30]	0.01	-1.21	[-2.31;-0.15]	0.02
	NEAs	-1.52	[-2.53;-0.70]	$<10^{-3}$	-1.89	[-2.87;-0.71]	0.003	-2.04	[-3.61;-0.73]	0.003

Table B8. CO relative trends in %.yr^{-1} during all the year, and during each season in the UT. From left to right, the anomalies are taken from deseasonalised P05, monthly means and P95. The insignificant trends with respect to the 95 % confidence level are indicated as NS. Note that the trends in WNAm are available only in DJF.

SEASON	REGION	P05			MEAN			P95		
(%.yr^{-1})		Slope	Conf. int. (95%)	p-value	Slope	Conf. int. (95%)	p-value	Slope	Conf. int. (95%)	p-value
DJF	WNAm		NS		-2.23	[-3.73;-0.94]	0.02	-2.29	[-4.34;-0.78]	0.003
	EUS		NS		-1.51	[-3.04;-0.63]	<10^{-3}	-1.86	[-2.63;-1.09]	<10^{-3}
	NAt		NS		-1.65	[-3.19;-0.75]	0.007	-2.20	[-3.45;-1.20]	0.005
	Eur	-1.59	[-2.98;-0.47]	0.01	-1.49	[-2.77;-0.67]	0.007	-1.75	[-2.88;-0.97]	0.007
	WMed		NS			NS			NS	
	MidE		NS		-1.25	[-3.99;-0.07]	0.05		NS	
	Sib	-1.17	[-2.64;-0.18]	0.035	-1.67	[-2.44;-0.33]	0.023	-1.11	[-2.51;-0.30]	0.025
	NEAs	-3.14	[-4.15;-1.94]	<10^{-3}	-2.56	[-4.31;-0.65]	0.01		NS	
MAM	EUS	-2.43	[-3.84;-1.27]	<10^{-3}	-2.05	[-3.01;-1.41]	<10^{-3}	-2.05	[-2.97;-0.76]	0.017
	NAt	-2.32	[-4.70;-0.97]	0.013	-1.97	[-3.24;-1.16]	0.003		NS	
	Eur	-1.53	[-3.10;-0.33]	0.017	-1.49	[-3.03;-1.12]	0.003	-1.65	[-3.00;-1.23]	0.003
	WMed		NS			NS			NS	
	MidE		NS			NS			NS	
	Sib		NS			NS			NS	
	NEAs	-1.93	[-3.19;-0.02]	0.05	-2.95	[-4.91;-0.46]	0.03		NS	
JJA	EUS	-1.76	[-2.64;-1.07]	<10^{-3}	-1.32	[-1.99;-0.56]	0.003	-1.45	[-2.6;-0.26]	0.007
	NAt		NS			NS			NS	
	Eur	-1.30	[-2.55;-0.54]	0.007	-1.34	[-2.41;-0.38]	0.01	-1.46	[-2.43;-0.41]	0.017
	WMed		NS			NS			NS	
	MidE		NS			NS			NS	
	Sib		NS			NS			NS	
	NEAs		NS			NS			NS	
SON	EUS		NS			NS			NS	
	NAt		NS			NS			NS	
	Eur		NS		-1.14	[-1.96;-0.07]	0.023		NS	
	WMed		NS		-1.26	[-3.93;-0.17]	0.04	-1.09	[-4.83;-0.34]	0.018
	MidE		NS			NS			NS	
	Sib		NS			NS			NS	
	NEAs		NS			NS			NS	

References

Andela, N., Kaiser, J., Heil, A., van Leeuwen, T. T., Wooster, M. J., van der Werf, G. R., Remy, S., and Schultz, M. G.: Assessment of the Global Fire Assimilation System (GFASv1), 2013.

Angelbratt, J., Mellqvist, J., Simpson, D., Jonson, J. E., Blumenstock, T., Borsdorff, T., Duchatelet, P., Forster, F., Hase, F., Mahieu, E., De Mazière, M., Notholt, J., Petersen, A. K., Raffalski, U., Servais, C., Sussmann, R., Warneke, T., and Vigouroux, C.: Carbon monoxide (CO) and ethane (C_2H_6) trends from ground-based solar FTIR measurements at six European stations, comparison and sensitivity analysis with the EMEP model, Atmos. Chem. Phys., 11, 9253–9269, doi:10.5194/acp-11-9253-2011, 2011.

Barret, B., Sauvage, B., Bennouna, Y., and Le Flochmoen, E.: Upper-tropospheric CO and O_3 budget during the Asian summer monsoon, Atmos. Chem. Phys., 16, 9129–9147, doi:10.5194/acp-16-9129-2016, 2016.

Boothe, A. C. and Homeyer, C. R.: Global large-scale stratosphere–troposphere exchange in modern reanalyses, Atmos. Chem. Phys., 17, 5537–5559, doi:10.5194/acp-17-5537-2017, 2017.

Bremer, H., Kar, J., Drummond, J. R., Nichitu, F., Zou, J., Liu, J., Gille, J. C., Deeter, M. N., Francis, G., Ziskin, D., and Warner, J.: Spatial and temporal variation of MOPITT CO in Africa and South America: A comparison with SHADOZ ozone and MODIS aerosol, J. Geophys. Res.-Atmos., 109, doi:10.1029/2003JD004234, 2004.

Butchart, N.: The Brewer-Dobson circulation, Rev. Geophys., 52, 157–184, doi:10.1002/2013RG000448, 2014.

Cammas, J.-P., Brioude, J., Chaboureau, J.-P., Duron, J., Mari, C., Mascart, P., Nédélec, P., Smit, H., Pätz, H.-W., Volz-Thomas, A., Stohl, A., and Fromm, M.: Injection in the lower stratosphere of biomass fire emissions followed by long-range transport: a MOZAIC case study, Atmos. Chem. Phys., 9, 5829–5846, doi:10.5194/acp-9-5829-2009, 2009.

Carslaw, D. C. and Ropkins, K.: openair - An R package for air quality data analysis, Environ. Modell. Softw., 27-28, 52–61, doi:10.1016/j.envsoft.2011.09.008, 2012.

Clark, H., Sauvage, B., Thouret, V., Nédélec, P., Blot, R., Wang, K.-Y., Smit, H., Neis, P., Petzold, A., Athier, G., Boulanger, D., Cousin, J.-M., Beswick, K., Gallagher, M., Baumgardner, D., Kaiser, J., Flaud, J.-M., Wahner, A., Volz-Thomas, A., and Cammas, J.-P.: The first regular measurements of ozone, carbon monoxide and water vapour in the Pacific UTLS by IAGOS, Tellus B, 67, doi:10.3402/tellusb.v67.28385, 2015.

Cooper, O., Parrish, D., Ziemke, J., Balashov, N., Cupeiro, M., Galbally, I., Gilge, S., Horowitz, L., Jensen, N., Lamarque, J., et al.: Global distribution and trends of tropospheric ozone: An observation-based review, doi:10.12952/journal.elementa.000029, 2014.

Cooper, O. R., Trainer, M., Thompson, A. M., Oltmans, S. J., Tarasick, D. W., Witte, J. C., Stohl, A., Eckhardt, S., Lelieveld, J., Newchurch, M. J., Johnson, B. J., Portmann, R. W., Kalnajs, L., Dubey, M. K., Leblanc, T., McDermid, I. S., Forbes, G., Wolfe, D., Carey-Smith, T., Morris, G. A., Lefer, B., Rappenglück, B., Joseph, E., Schmidlin, F., Meagher, J., Fehsenfeld, F. C., Keating, T. J., Van Curen, R. A., and Minschwaner, K.: Evidence for a recurring eastern North America upper tropospheric ozone maximum during summer, J. Geophys. Res.-Atmos., 112, doi:10.1029/2007JD008710, d23304, 2007.

Cooper, O. R., Eckhardt, S., Crawford, J. H., Brown, C. C., Cohen, R. C., Bertram, T. H., Wooldridge, P., Perring, A., Brune, W. H., Ren, X., Brunner, D., and Baughcum, S. L.: Summertime buildup and decay of lightning NOx and aged thunderstorm outflow above North America, J. Geophys. Res.-Atmos., 114, doi:10.1029/2008JD010293, d01101, 2009.

Cooper, O. R., Parrish, D. D., Stohl, A., Trainer, M., Nédélec, P., Thouret, V., Cammas, J.-P., Oltmans, S. J., Johnson, B. J., Tarasick, D. W., Leblanc, T., McDermid, I. S., Jaffe, D., Gao, R., Stith, J., Ryerson, T., Aikin, K., Campos, T., Weinheimer, A., and Avery, M. A.: Increasing

springtime ozone mixing ratios in the free troposphere over western North America, Nat. Geosci., 463, 344–348, doi:10.1038/nature08708, 2010.

Ebojie, F., von Savigny, C., Ladstätter-Weißenmayer, A., Rozanov, A., Weber, M., Eichmann, K.-U., Bötel, S., Rahpoe, N., Bovensmann, H., and Burrows, J. P.: Tropospheric column amount of ozone retrieved from SCIAMACHY limb–nadir-matching observations, Atmos. Meas. Tech., 7, 2073–2096, doi:10.5194/amt-7-2073-2014, 2014.

Ebojie, F., Burrows, J. P., Gebhardt, C., Ladstätter-Weißenmayer, A., von Savigny, C., Rozanov, A., Weber, M., and Bovensmann, H.: Global tropospheric ozone variations from 2003 to 2011 as seen by SCIAMACHY, Atmos. Chem. Phys., 16, 417–436, doi:10.5194/acp-16-417-2016, 2016.

Edwards, D. P., Emmons, L. K., Hauglustaine, D. A., Chu, D. A., Gille, J. C., Kaufman, Y. J., Pétron, G., Yurganov, L. N., Giglio, L., Deeter, M. N., Yudin, V., Ziskin, D. C., Warner, J., Lamarque, J.-F., Francis, G. L., Ho, S. P., Mao, D., Chen, J., Grechko, E. I., and Drummond, J. R.: Observations of carbon monoxide and aerosols from the Terra satellite: Northern Hemisphere variability, J. Geophys. Res.-Atmos., 109, doi:10.1029/2004JD004727, 2004.

Elguindi, N., Clark, H., Ordóñez, C., Thouret, V., Flemming, J., Stein, O., Huijnen, V., Moinat, P., Inness, A., Peuch, V.-H., Stohl, A., Turquety, S., Athier, G., Cammas, J.-P., and Schultz, M.: Current status of the ability of the GEMS/MACC models to reproduce the tropospheric CO vertical distribution as measured by MOZAIC, Geosci. Model Dev., 3, 501–518, doi:10.5194/gmd-3-501-2010, 2010.

Garfinkel, C. I., Aquila, V., Waugh, D. W., and Oman, L. D.: Time-varying changes in the simulated structure of the Brewer–Dobson Circulation, Atmos. Chem. Phys., 17, 1313–1327, doi:10.5194/acp-17-1313-2017, 2017.

Gaudel, A. and Cooper, O. R.: Tropospheric Ozone Assessment Report: Present-day distribution and trends of tropospheric ozone relevant to climate and global atmospheric chemistry model evaluation, Elem. Sci. Anth., in preparation, 2017.

Gaudel, A., Ancellet, G., and Godin-Beekmann, S.: Analysis of 20 years of tropospheric ozone vertical profiles by lidar and ECC at Observatoire de Haute Provence (OHP) at 44°N, 6.7°E, Atmos. Environ., 113, 78 – 89, doi:10.1016/j.atmosenv.2015.04.028, 2015a.

Gaudel, A., Clark, H., Thouret, V., Jones, L., Inness, A., Flemming, J., Stein, O., Huijnen, V., Eskes, H., Nédélec, P., and Boulanger, D.: On the use of MOZAIC-IAGOS data to assess the ability of the MACC reanalysis to reproduce the distribution of ozone and CO in the UTLS over Europe, Tellus B, 67, 27 955, doi:10.3402/tellusb.v67.27955, 2015b.

Gettelman, A., Hegglin, M. I., Son, S.-W., Kim, J., Fujiwara, M., Birner, T., Kremser, S., Rex, M., Añel, J. A., Akiyoshi, H., Austin, J., Bekki, S., Braesike, P., Brühl, C., Butchart, N., Chipperfield, M., Dameris, M., Dhomse, S., Garny, H., Hardiman, S. C., Jöckel, P., Kinnison, D. E., Lamarque, J. F., Mancini, E., Marchand, M., Michou, M., Morgenstern, O., Pawson, S., Pitari, G., Plummer, D., Pyle, J. A., Rozanov, E., Scinocca, J., Shepherd, T. G., Shibata, K., Smale, D., Teyssèdre, H., and Tian, W.: Multimodel assessment of the upper troposphere and lower stratosphere: Tropics and global trends, J. Geophys. Res.-Atmos., 115, doi:10.1029/2009JD013638, d00M08, 2010.

Gettelman, A., Hoor, P., Pan, L. L., Randel, W. J., Hegglin, M. I., and Birner, T.: The extratropical upper troposphere and lower stratosphere, Rev. Geophys., 49, doi:10.1029/2011RG000355, rG3003, 2011.

Granados-Muñoz, M. J., Johnson, M. S., and Leblanc, T.: Influence of the North American monsoon on Southern California tropospheric ozone levels during summer in 2013 and 2014, Geophys. Res. Lett., 44, 6431–6439, doi:10.1002/2017GL073375, 2017GL073375, 2017.

Granados-Muñoz, M. J. and Leblanc, T.: Tropospheric ozone seasonal and long-term variability as seen by lidar and surface measurements at the JPL-Table Mountain Facility, California, Atmos. Chem. Phys., 16, 9299–9319, doi:10.5194/acp-16-9299-2016, 2016.

Granier, C., Bessagnet, B., Bond, T., D'Angiola, A., van der Gon, H., Frost, G. J., Heil, A., Kaiser, J. W., Kinne, S., Klimont, Z., Kloster, S., Lamarque, J.-F., Liousse, C., Masui, T., Meleux, F., Mieville, A., Ohara, T., Raut, J.-C., Riahi, K., Schultz, M. G., Smith, S. J., Thompson,

A., van Aardenne, J., van der Werf, G. R., and van Vuuren, D. P.: Evolution of anthropogenic and biomass burning emissions of air pollutants at global and regional scales during the 1980–2010 period, Climatic Change, 109, 163, doi:10.1007/s10584-011-0154-1, 2011.

Gratz, L., Jaffe, D., and Hee, J.: Causes of increasing ozone and decreasing carbon monoxide in springtime at the Mt. Bachelor Observatory from 2004 to 2013, Atmos. Environ., 109, 323–330, doi:10.1016/j.atmosenv.2014.05.076, 2015.

Gressent, A., Sauvage, B., Defer, E., Pätz, H. W., Thomas, K., Holle, R., Cammas, J.-P., Nédélec, P., Boulanger, D., Thouret, V., and Volz-Thomas, A.: Lightning NOx influence on large-scale NOy and O3 plumes observed over the northern mid-latitudes, Tellus B, 66, 25 544, doi:10.3402/tellusb.v66.25544, 2014.

Helten, M., Smit, H. G. J., Sträter, W., Kley, D., Nédélec, P., Zöger, M., and Busen, R.: Calibration and performance of automatic compact instrumentation for the measurement of relative humidity from passenger aircraft, J. Geophys. Res.-Atmos., 103, 25 643–25 652, doi:10.1029/98JD00536, 1998.

Hsu, J. and Prather, M. J.: Stratospheric variability and tropospheric ozone, J. Geophys. Res.-Atmos., 114, doi:10.1029/2008JD010942, d06102, 2009.

Huang, L., Jiang, J. H., Murray, L. T., Damon, M. R., Su, H., and Livesey, N. J.: Evaluation of UTLS carbon monoxide simulations in GMI and GEOS-Chem chemical transport models using Aura MLS observations, Atmos. Chem. Phys., 16, 5641–5663, doi:10.5194/acp-16-5641-2016, 2016.

Hudman, R. C., Jacob, D. J., Cooper, O. R., Evans, M. J., Heald, C. L., Park, R. J., Fehsenfeld, F., Flocke, F., Holloway, J., Hübler, G., Kita, K., Koike, M., Kondo, Y., Neuman, A., Nowak, J., Oltmans, S., Parrish, D., Roberts, J. M., and Ryerson, T.: Ozone production in transpacific Asian pollution plumes and implications for ozone air quality in California, J. Geophys. Res.-Atmos., 109, doi:10.1029/2004JD004974, d23S10, 2004.

IPCC: Climate change 2013: The physical science basis, Tech. rep., http://www.ipcc.ch/report/ar5/wg1/, 2013.

Jiang, J. H., Livesey, N. J., Su, H., Neary, L., McConnell, J. C., and Richards, N. A. D.: Connecting surface emissions, convective uplifting, and long-range transport of carbon monoxide in the upper troposphere: New observations from the Aura Microwave Limb Sounder, Geophys. Res. Lett., 34, doi:10.1029/2007GL030638, l18812, 2007.

Jiang, Z., Worden, J. R., Worden, H., Deeter, M., Jones, D. B. A., Arellano, A. F., and Henze, D. K.: A fifteen year record of CO emissions constrained by MOPITT CO observations, Atmos. Chem. Phys. Discuss., pp. 1–46, doi:10.5194/acp-2016-811, 2017.

Koumoutsaris, S., Bey, I., Generoso, S., and Thouret, V.: Influence of El Niño–Southern Oscillation on the interannual variability of tropospheric ozone in the northern midlatitudes, J. Geophys. Res.-Atmos., 113, doi:10.1029/2007JD009753, d19301, 2008.

Laken, B. A. and Shahbaz, T.: Satellite-Detected Carbon Monoxide Pollution during 2000–2012: Examining Global Trends and also Regional Anthropogenic Periods over China, the EU and the USA, Climate, 2, 1, doi:10.3390/cli2010001, 2014.

Lelieveld, J., Gromov, S., Pozzer, A., and Taraborrelli, D.: Global tropospheric hydroxyl distribution, budget and reactivity, Atmos. Chem. Phys., 16, 12 477–12 493, doi:10.5194/acp-16-12477-2016, 2016.

Liu, J., Logan, J. A., Jones, D. B. A., Livesey, N. J., Megretskaia, I., Carouge, C., and Nedelec, P.: Analysis of CO in the tropical troposphere using Aura satellite data and the GEOS-Chem model: insights into transport characteristics of the GEOS meteorological products, Atmos. Chem. Phys., 10, 12 207–12 232, doi:10.5194/acp-10-12207-2010, 2010.

Livesey, N. J., Logan, J. A., Santee, M. L., Waters, J. W., Doherty, R. M., Read, W. G., Froidevaux, L., and Jiang, J. H.: Interrelated variations of O_3, CO and deep convection in the tropical/subtropical upper troposphere observed by the Aura Microwave Limb Sounder (MLS) during 2004–2011, Atmos. Chem. Phys., 13, 579–598, doi:10.5194/acp-13-579-2013, 2013.

Logan, J. A., Prather, M. J., Wofsy, S. C., and McElroy, M. B.: Tropospheric chemistry: A global perspective, J. Geophys. Res.-Oceans, 86, 7210–7254, doi:10.1029/JC086iC08p07210, 1981.

Logan, J. A., Staehelin, J., Megretskaia, I. A., Cammas, J.-P., Thouret, V., Claude, H., De Backer, H., Steinbacher, M., Scheel, H.-E., Stübi, R., Fröhlich, M., and Derwent, R.: Changes in ozone over Europe: Analysis of ozone measurements from sondes, regular aircraft (MOZAIC) and alpine surface sites, J. Geophys. Res.-Atmos., 117, doi:10.1029/2011JD016952, 2012.

Madonna, E., Wernli, H., Joos, H., and Martius, O.: Warm Conveyor Belts in the ERA-Interim Dataset (1979–2010). Part I: Climatology and Potential Vorticity Evolution, J. Climate, 27, 3–26, doi:10.1175/JCLI-D-12-00720.1, 2014.

Marenco, A., Thouret, V., Nédélec, P., Smit, H., Helten, M., Kley, D., Karsher, F., Simon, P., Law, K., Pyle, J., Poschmann, G., Von Wrede, R., Hume, C., and Cook, T.: Measurement of ozone and water vapour by Airbus in-service aircraft : The MOZAIC airborne programme, an overview, J. Geophys. Res., 103, 25 631–25 642, doi:10.1029/98JD00977, 1998.

Monks, P. S., Archibald, A. T., Colette, A., Cooper, O., Coyle, M., Derwent, R., Fowler, D., Granier, C., Law, K. S., Mills, G. E., Stevenson, D. S., Tarasova, O., Thouret, V., von Schneidemesser, E., Sommariva, R., Wild, O., and Williams, M. L.: Tropospheric ozone and its precursors from the urban to the global scale from air quality to short-lived climate forcer, Atmos. Chem. Phys., 15, 8889–8973, doi:10.5194/acp-15-8889-2015, 2015.

Nédélec, P., Cammas, J.-P., Thouret, V., Athier, G., and Cousin, J.-M.: An improved infrared carbon monoxide analyser for routine measurements aboard commercial Airbus aircraft: technical validation and first scientific results of the MOZAIC III programme, Atmos. Chem. Phys., 3, 1551–1564, doi:10.5194/acp-3-1551-2003, 2003.

Nédélec, P., Thouret, V., Brioude, J., Sauvage, B., Cammas, J.-P., and Stohl, A.: Extreme CO concentrations in the upper troposphere over northeast Asia in June 2003 from the in situ MOZAIC aircraft data, Geophys. Res. Lett., 32, doi:10.1029/2005GL023141, l14807, 2005.

Nédélec, P., Blot, R., Boulanger, D., Athier, G., Cousin, J.-M., Gautron, B., Petzold, A., Volz-Thomas, A., and Thouret, V.: Instrumentation on commercial aircraft for monitoring the atmospheric composition on a global scale: the IAGOS system, technical overview of ozone and carbon monoxide measurements, Tellus B, 67, 27 791, doi:10.3402/tellusb.v67.27791, 2015.

Neu, J. L., Flury, T., Manney, G. L., Santee, M. L., Livesey, N. J., and Worden, J.: Tropospheric ozone variations governed by changes in stratospheric circulation, Nat. Geosci., 7, 340–344, doi:10.1038/ngeo2138, 2014a.

Neu, J. L., Hegglin, M. I., Tegtmeier, S., Bourassa, A., Degenstein, D., Froidevaux, L., Fuller, R., Funke, B., Gille, J., Jones, A., Rozanov, A., Toohey, M., von Clarmann, T., Walker, K. A., and Worden, J. R.: The SPARC Data Initiative: Comparison of upper troposphere/lower stratosphere ozone climatologies from limb-viewing instruments and the nadir-viewing Tropospheric Emission Spectrometer, J. Geophys. Res.-Atmos., 119, 6971–6990, doi:10.1002/2013JD020822, 2013JD020822, 2014b.

Olsen, M. A., Schoeberl, M. R., and Douglass, A. R.: Stratosphere-troposphere exchange of mass and ozone, J. Geophys. Res.-Atmos., 109, doi:10.1029/2004JD005186, 2004.

Olsen, M. A., Douglass, A. R., and Kaplan, T. B.: Variability of extratropical ozone stratosphere-troposphere exchange using microwave limb sounder observations, J. Geophys. Res.-Atmos., 118, 1090–1099, doi:10.1029/2012JD018465, 2013.

Oltmans, S., Lefohn, A., Shadwick, D., Harris, J., Scheel, H., Galbally, I., Tarasick, D., Johnson, B., Brunke, E.-G., Claude, H., Zeng, G., Nichol, S., Schmidlin, F., Davies, J., Cuevas, E., Redondas, A., Naoe, H., Nakano, T., and Kawasato, T.: Recent tropospheric ozone changes – A pattern dominated by slow or no growth, Atmos. Environ., 67, 331–351, doi:10.1016/j.atmosenv.2012.10.057, 2013.

Osman, M. K., Tarasick, D. W., Liu, J., Moeini, O., Thouret, V., Fioletov, V. E., Parrington, M., and Nédélec, P.: Carbon monoxide climatology derived from the trajectory mapping of global MOZAIC-IAGOS data, Atmos. Chem. Phys., 16, 10 263–10 282, doi:10.5194/acp-16-10263-2016, 2016.

Park, M., Randel, W. J., Gettelman, A., Massie, S. T., and Jiang, J. H.: Transport above the Asian summer monsoon anticyclone inferred from Aura Microwave Limb Sounder tracers, J. Geophys. Res.-Atmos., 112, doi:10.1029/2006JD008294, d16309, 2007.

Park, M., Randel, W. J., Emmons, L. K., and Livesey, N. J.: Transport pathways of carbon monoxide in the Asian summer monsoon diagnosed from Model of Ozone and Related Tracers (MOZART), J. Geophys. Res.-Atmos., 114, doi:10.1029/2008JD010621, d08303, 2009.

Petetin, H., Thouret, V., Fontaine, A., Sauvage, B., Athier, G., Blot, R., Boulanger, D., Cousin, J.-M., and Nédélec, P.: Characterizing tropospheric ozone and CO around Frankfurt between 1994–2012 based on MOZAIC–IAGOS aircraft measurements, Atmos. Chem. Phys., 16, 15 147–15 163, doi:10.5194/acp-16-15147-2016, 2016.

Petzold, A., Thouret, V., Gerbig, C., Zahn, A., Brenninkmeijer, C., Gallagher, M., Hermann, M., Pontaud, M., Ziereis, H., Boulanger, D., Marshall, J., Nédélec, P., Smit, H., Friess, U., Flaud, J.-M., Wahner, A., Cammas, J.-P., and Volz-Thomas, A.: Global-scale atmosphere monitoring by in-service aircraft - current achievements and future prospects of the European Research Infrastructure IAGOS, Tellus B, 67, doi:10.3402/tellusb.v67.28452, 2015.

Ricaud, P., Sič, B., El Amraoui, L., Attié, J.-L., Zbinden, R., Huszar, P., Szopa, S., Parmentier, J., Jaidan, N., Michou, M., Abida, R., Carminati, F., Hauglustaine, D., August, T., Warner, J., Imasu, R., Saitoh, N., and Peuch, V.-H.: Impact of the Asian monsoon anticyclone on the variability of mid-to-upper tropospheric methane above the Mediterranean Basin, Atmos. Chem. Phys., 14, 11 427–11 446, doi:10.5194/acp-14-11427-2014, 2014.

Riese, M., Ploeger, F., Rap, A., Vogel, B., Konopka, P., Dameris, M., and Forster, P.: Impact of uncertainties in atmospheric mixing on simulated UTLS composition and related radiative effects, J. Geophys. Res., 117, D16 305, doi:10.1029/2012JD017751, 2012.

Sauvage, B., Thouret, V., Cammas, J.-P., Gheusi, F., Athier, G., and Nédélec, P.: Tropospheric ozone over Equatorial Africa: regional aspects from the MOZAIC data, Atmos. Chem. Phys., 5, 311–335, doi:10.5194/acp-5-311-2005, 2005.

Sauvage, B., Martin, R. V., van Donkelaar, A., Liu, X., Chance, K., Jaeglé, L., Palmer, P. I., Wu, S., and Fu, T.-M.: Remote sensed and in situ constraints on processes affecting tropical tropospheric ozone, Atmos. Chem. Phys., 7, 815–838, doi:10.5194/acp-7-815-2007, 2007a.

Sauvage, B., Martin, R. V., van Donkelaar, A., and Ziemke, J. R.: Quantification of the factors controlling tropical tropospheric ozone and the South Atlantic maximum, J. Geophys. Res.-Atmos., 112, doi:10.1029/2006JD008008, d11309, 2007b.

Sauvage, B., Thouret, V., Cammas, J.-P., Brioude, J., Nédélec, P., and Mari, C.: Meridional ozone gradients in the African upper troposphere, Geophys. Res. Lett., 34, doi:10.1029/2006GL028542, l03817, 2007c.

Sauvage, B., Fontaine, A., Eckhardt, S., Auby, A., Boulanger, D., Petetin, H., Paugam, R., Athier, G., Cousin, J.-M., Darras, S., Nédélec, P., Stohl, A., Turquety, S., Cammas, J.-P., and Thouret, V.: Source attribution using FLEXPART and carbon monoxide emission inventories: SOFT-IO version 1.0, Atmos. Chem. Phys. Discuss., doi:10.5194/acp-2017-653, 2017.

Sen, P. K.: Estimates of the Regression Coefficient Based on Kendall's Tau, J. Am. Stat. Assoc., 63, 1379–1389, doi:10.1080/01621459.1968.10480934, 1968.

Stevenson, D. S., Young, P. J., Naik, V., Lamarque, J.-F., Shindell, D. T., Voulgarakis, A., Skeie, R. B., Dalsoren, S. B., Myhre, G., Berntsen, T. K., Folberth, G. A., Rumbold, S. T., Collins, W. J., MacKenzie, I. A., Doherty, R. M., Zeng, G., van Noije, T. P. C., Strunk, A., Bergmann, D., Cameron-Smith, P., Plummer, D. A., Strode, S. A., Horowitz, L., Lee, Y. H., Szopa, S., Sudo, K., Nagashima, T., Josse, B., Cionni, I., Righi, M., Eyring, V., Conley, A., Bowman, K. W., Wild, O., and Archibald, A.: Tropospheric ozone changes, radiative forcing and attribution to emissions in the Atmospheric Chemistry and Climate Model Intercomparison Project (ACCMIP), Atmos. Chem. Phys., 13, 3063–3085, doi:10.5194/acp-13-3063-2013, 2013.

Stratmann, G., Ziereis, H., Stock, P., Brenninkmeijer, C., Zahn, A., Rauthe-Schöch, A., Velthoven, P., Schlager, H., and Volz-Thomas, A.: {NO} and {NOy} in the upper troposphere: Nine years of {CARIBIC} measurements onboard a passenger aircraft, Atmos. Environ., 133, 93–111, doi:10.1016/j.atmosenv.2016.02.035, 2016.

5   Tang, Q., Hess, P. G., Brown-Steiner, B., and Kinnison, D. E.: Tropospheric ozone decrease due to the Mount Pinatubo eruption: Reduced stratospheric influx, Geophys. Res. Lett., 40, 5553–5558, doi:10.1002/2013GL056563, 2013.

Tanimoto, H., Okamoto, S., Ikeda, K., Thouret, V., Emmons, L. K., Tilmes, S., Lamarque, J.-F., and Gaubert, B.: Free tropospheric ozone trends over East Asia from 1991 to 2015: Flattening in the lower troposphere and increasing in the upper troposphere, Geophys. Res. Lett., in preparation, 2017.

10   Tereszchuk, K. A., Moore, D. P., Harrison, J. J., Boone, C. D., Park, M., Remedios, J. J., Randel, W. J., and Bernath, P. F.: Observations of peroxyacetyl nitrate (PAN) in the upper troposphere by the Atmospheric Chemistry Experiment-Fourier Transform Spectrometer (ACE-FTS), Atmos. Chem. Phys., 13, 5601–5613, doi:10.5194/acp-13-5601-2013, 2013.

Thompson, A. M., Witte, J. C., Oltmans, S. J., Schmidlin, F. J., Logan, J. A., Fujiwara, M., Kirchhoff, V. W. J. H., Posny, F., Coetzee, G. J. R., Hoegger, B., Kawakami, S., Ogawa, T., Fortuin, J. P. F., and Kelder, H. M.: Southern Hemisphere Additional Ozonesondes
15   (SHADOZ) 1998–2000 tropical ozone climatology 2. Tropospheric variability and the zonal wave-one, J. Geophys. Res.-Atmos., 108, doi:10.1029/2002JD002241, 8241, 2003.

Thouret, V., Marenco, A., Logan, J. A., Nédélec, P., and Grouhel, C.: Comparisons of ozone measurements from the MOZAIC airborne program and the ozone sounding network at eight locations, J. Geophys. Res., 103, 25 695–25 720, doi:10.1029/98JD02243, 1998.

Thouret, V., Cammas, J.-P., Sauvage, B., Athier, G., Zbinden, R. M., Nédélec, P., Simon, P., and Karcher, F.: Tropopause referenced ozone cli-
20   matology and inter-annual variability (1994–2003) from the MOZAIC programme, Atmos. Chem. Phys., 6, 1033–1051, doi:10.5194/acp-6-1033-2006, 2006.

Tilmes, S., Pan, L. L., Hoor, P., Atlas, E., Avery, M. A., Campos, T., Christensen, L. E., Diskin, G. S., Gao, R.-S., Herman, R. L., Hintsa, E. J., Loewenstein, M., Lopez, J., Paige, M. E., Pittman, J. V., Podolske, J. R., Proffitt, M. R., Sachse, G. W., Schiller, C., Schlager, H., Smith, J., Spelten, N., Webster, C., Weinheimer, A., and Zondlo, M. A.: An aircraft-based upper troposphere lower stratosphere O_3, CO,
25   and H_2O climatology for the Northern Hemisphere, J. Geophys. Res.-Atmos., 115, doi:10.1029/2009JD012731, d14303, 2010.

Tyrlis, E., Lelieveld, J., and Steil, B.: The summer circulation over the eastern Mediterranean and the Middle East: influence of the South Asian monsoon, Climate Dynamics, 40, 1103–1123, doi:10.1007/s00382-012-1528-4, 2013.

Verstraeten, W. W., Boersma, K. F., Zörner, J., Allaart, M. A. F., Bowman, K. W., and Worden, J. R.: Validation of six years of TES tropospheric ozone retrievals with ozonesonde measurements: implications for spatial patterns and temporal stability in the bias, Atmos.
30   Meas. Tech., 6, 1413–1423, doi:10.5194/amt-6-1413-2013, 2013.

Škerlak, B., Sprenger, M., and Wernli, H.: A global climatology of stratosphere–troposphere exchange using the ERA-Interim data set from 1979 to 2011, Atmos. Chem. Phys., 14, 913–937, doi:10.5194/acp-14-913-2014, 2014.

Worden, H. M., Deeter, M. N., Frankenberg, C., George, M., Nichitiu, F., Worden, J., Aben, I., Bowman, K. W., Clerbaux, C., Coheur, P. F., de Laat, A. T. J., Detweiler, R., Drummond, J. R., Edwards, D. P., Gille, J. C., Hurtmans, D., Luo, M., Martìnez-Alonso, S.,
35   Massie, S., Pfister, G., and Warner, J. X.: Decadal record of satellite carbon monoxide observations, Atmos. Chem. Phys., 13, 837–850, doi:10.5194/acp-13-837-2013, 2013.

Yamasoe, M., Sauvage, B., Thouret, V., Nédélec, P., Le Flochmoen, E., and Barret, B.: Analysis of tropospheric ozone and carbon monoxide profiles over South America based on MOZAIC/IAGOS database and model simulations, Tellus B, 67, doi:10.3402/tellusb.v67.27884, 2015.

Zanis, P., Hadjinicolaou, P., Pozzer, A., Tyrlis, E., Dafka, S., Mihalopoulos, N., and Lelieveld, J.: Summertime free-tropospheric ozone pool over the eastern Mediterranean/Middle East, Atmos. Chem. Phys., 14, 115–132, doi:10.5194/acp-14-115-2014, 2014.

Zbinden, R. M., Thouret, V., Ricaud, P., Carminati, F., Cammas, J.-P., and Nédélec, P.: Climatology of pure Tropospheric profiles and column contents of ozone and carbon monoxide using MOZAIC in the mid-northern latitudes (24 N to 50 N) from 1994 to 2009, Atmos. Chem. Phys., 13, 12 363–12 388, doi:10.5194/acp-13-12363-2013, 2013.

Zhang, Y., Cooper, O. R., Gaudel, A., Thompson, A. M., Nédélec, P., Ogino, S.-Y., and West, J. J.: Tropospheric ozone change from 1980 to 2010 dominated by equatorward redistribution of emissions, Nat. Geosci., 9, 875–879, doi:10.1038/NGEO2827, 2016.

Ziemke, J. R., Chandra, S., Labow, G. J., Bhartia, P. K., Froidevaux, L., and Witte, J. C.: A global climatology of tropospheric and strato-spheric ozone derived from Aura OMI and MLS measurements, Atmos. Chem. Phys., 11, 9237–9251, doi:10.5194/acp-11-9237-2011, 2011.